Combining homogeneous and heterogeneous chemistry to model inorganic compounds concentrations in indoor environments: the H^{2}I model (v1.0)

Eve-Agnès Fiorentino[1], Henri Wortham[1], and Karine Sartelet[2]

[1] Laboratory of Environmental Chemistry, CNRS-UMR 7376, Aix-Marseille Université, Marseille, France
[2] CEREA, Joint Laboratory Ecole des Ponts ParisTech - EdF R&D, Université Paris-Est, Champs-sur-Marne, France

Correspondence: eve-agnes.fiorentino@univ-amu.fr

Abstract. Homogeneous reactivity has been extensively studied over the past years through outdoor air-quality simulations. However, indoor atmospheres are known to be largely influenced by another type of chemistry, that is reactivity with surfaces. Despite progress in the understanding of heterogeneous reactions, these remain barely integrated in numerical models. In this paper, a room-scale indoor air-quality (IAQ) model is developed to represent both heterogeneous and homogeneous

5 chemistry. Thanks to the introduction of sorbed species, deposition and surface reactivity are treated as two separate processes, and desorption reactions are incorporated. The simulated concentrations of inorganic species are compared to experimental measurements acquired in a real room, thus allowing to calibrate the model's undetermined parameters. For the considered experiments durations, the influence of the simulations initial conditions is strong. The model succeeds in simulating correctly the four inorganic species concentrations that were measured, namely NO, NO$_2$, HONO and O$_3$, together with the HOx (HO +

10 HO$_2$) radicals. Each parameter is then varied to estimate its sensitivity and identify the most prevailing processes. The speed of air and building filtration factor are uncertain parameters which appear to have a strong influence, the first one on deposition, and the second one on the control of transport from outdoor. As expected, the NO$_2$ surface hydrolysis plays a key role in the production of secondary species. The secondary production of NO by the reaction of sorbed HONO with sorbed HNO$_3$ stands as an essential component to integrate in IAQ models.

1 Introduction

At a time where sustainable development requires more efforts than ever, the improvement of building isolation has become a major concern in the field of construction and renovation. Apart from being necessary for the health and comfort of the occupants, airtight conceptions are needed to curb the energy consumption of accommodations and offices, and thus decrease

20 their carbon footprint. However, as air remains more confined with a lower exchange rate with the outdoor, the pollutants generated indoors have less possibilities to escape, which raises health matters. It is now established that indoor atmospheres

are more polluted than outdoors, while we spend most of our time in indoor environments, up to 90% in developed countries (Carslaw, 2007). In this context, indoor air-quality (IAQ) is bound to be an increasingly studied issue.

Whereas numerical simulations appear as a standard approach for the study of outdoor atmospheres, they are less common in
25   the field of indoor environments. Indoor environments are complex, and processes relying on the surface to volume ratio, which are still not fully understood but often negligible outdoors, get a predominant importance in indoor environments (Weschler, 2011).

Historically, early attempts to model indoor atmospheres focused on the correct assessment of primary emissions, considering each chemical component independently. The model of Nazaroff and Cass (1986) provided the first description of the
30   indoor environment as a chemically reactive homogeneous system, taking into account the interactions of about 30 species and groups of species based on a modified version of the Falls and Seinfeld (1978) mechanism. They included photolytic reactions and a simple form of deposition, considering decomposition and irreversible absorption reactions. Sarwar et al. (2002) adapted the chemical mechanism SAPRC-99 in order to take into account newer advances on O_3/alkenes reactions. In particular, they introduced the chemistry of 40 VOCs recognized as atmospheric pollutants. Deposition was modelled as in Nazaroff and Cass
35   (1986), and no deposition was assumed for species for which no deposition velocity was available. A more detailed chemical mechanism was tested by Carslaw (2007), who adapted the Master Chemical Mechanism (MCM) to indoor environments, including about 4600 species and 15400 reactions. Deposition was modelled similarly to Nazaroff and Cass (1986), and for the first time, a heterogeneous reaction on indoor surfaces was considered, by introducing a production rate accounting for HONO secondary formation. Later, Mendez et al. (2015) implemented a simplified version of the SAPRC-07 mechanism and
40   described deposition as a two-step process, by making a distinction between transport from free-space to surface, and reactivity with the surface. Further details were provided by Mendez et al. (2017), who parameterized the mass transfer effect using a model of transport-limited deposition velocity.

As underlined by Weschler (2011), surface chemistry is responsible for secondary pollutant formation which can be of greater importance for IAQ than the primary emissions. Because heterogeneous reactions can be faster than their equivalent gas-
45   phase homogeneous reaction, their importance relative to the air exchange rate and thus their influence on indoor atmospheres is large. Secondary pollutants can persist a long time after the reagent species have come to negligible levels, and are very difficult to anticipate, due to their strong dependence on ambiant conditions.

The heterogeneous hydrolysis of NO_2 is one of these reactions, and is recognized as the main source of HONO in indoor environments. There is evidence that certain surfaces can act as a reservoir of sorbed NO_2, and that these surfaces can release
50   HONO long after the decay of NO_2 (Wainman et al., 2001). Presumably, this HONO surface release depends on the ambiant NO_2 concentration, ambiant relative humidity and on the surface ability to retain water.

As a rule, it is assumed that the heterogeneous hydrolysis of NO_2 leads to the formation of HONO and HNO_3 following the stoichiometry proposed by Febo and Perrino (1991) :

$$2\,NO_2 + H_2O \rightarrow HONO + HNO_3. \tag{R1}$$

55   Contrary to HONO, HNO_3 is not observed as gas-phase product in this process, due to its strong adsorption capacity. HNO_3 remains on the surface and can react with other species. Namely, Mochida and Finlayson-Pitts (2000) studied the production of NO_2 by the reaction of HNO_3 with gaseous NO on porous glass. They showed that the NO concentration cannot decay below a threshold value, suggesting NO regeneration pathways. Coherently, NO formation was pointed out during NO_2 hydrolysis experiments, simultaneously to the NO_2 exposure or at longer reaction times. Finlayson-Pitts et al. (2003) measured for this

60   reaction a HONO yield that was much less than 50% of the NO_2 loss, and observed that the yield of NO relative to HONO increased with time. Based on their own and previously reported observations, they suggested NO could be formed by the secondary autoionization of the sorbed HONO such as

$$2\,HONO \rightarrow NO + NO_2 + H_2O \qquad\qquad (R2)$$

and also by conversion of the sorbed HONO following a mechanism that involves HNO_3 and simplifies to the net reaction

65    $$HONO + HNO_3 \rightarrow 2\,NO + H_2O + O_2. \qquad\qquad (R3)$$

Considering longer reaction times, NO could also react with HNO_3 following the reaction (Finlayson-Pitts et al., 2003)

$$NO + HNO_3 \rightarrow HONO + NO_2. \qquad\qquad (R4)$$

Finally, the photochemical enhancement of the NO_2 hydrolysis was investigated by Ramazan et al. (2004), who showed that the NO_2 hydrolysis was not photo-enhanced itself, but that HONO production was fostered by another process, which was

70   likely the photolysis of sorbed HNO_3 caused by the UV rays. Other heterogenous reactions could be pointed out, especially those involving O_3 which is known to have a significant adsorption capacity.

Reviewing the state of the art of surface reactions unveils a serious void in the modelling of indoor atmospheres. Current models incorporate these phenomena quite incompletely, due to the strong uncertainties they are subjected to. In particular, the ratio of production of NO compared to HONO during the NO_2 hydrolysis derives from mechanisms that are still unclear.

75   The detailed scheme proposed by Finlayson-Pitts et al. (2003) involves the reactions of several intermediate species whose reaction rates are unknown. As a test, they introduced this scheme in the kinetic program REACT to compute the loss of NO_2 and formation of HONO and NO, and adjusted the required rate constants to obtain a good match with their cell experiments data. In this model, uptake and reactions on surfaces were not explicitly treated, making heterogeneous reactions implemented like gas-phase reactions. Ramazan et al. (2004) made a similar work, and the parameterization they proposed was later used by

80   Courtey et al. (2009) to model confined atmospheres, *i.e.* without including ventilation and primary emissions.

In this work, a room-scale IAQ model is developed, to include the above described heterogeneous chemistry, in addition to the homogeneous chemistry already considered by box models. The concentrations simulated by this model are compared to measurements that were performed in a real office (Gandolfo, 2018) from the 27th to the 31st October 2016 in Martigues (France). The aim of these measurements was to study the impact of photocatalytic paints characterized in laboratory experi-

85   ments (Gandolfo et al., 2015, 2017) on indoor atmospheres healthiness. Whereas laboratory tests were conducted with paints containing up to 7% of TiO_2 nanoparticles, this campaign was restricted to the use of a non-photocatalytic paint (reference

paint), and to the same paint enriched with a commercially viable amount of 3.5% of TiO_2 nanoparticles. Two types of measurements were obtained, with UVs-blocking and borosilicate windows. The simulations presented in this paper are compared to the data obtained with the UVs-blocking window only, so as to minimize the effect of photo-induced processes, which will

90 be studied in a separate paper. The organic compounds concentrations are fixed to their measured values, so as to focus on the modelling of inorganic species.

The present model, called H^2I (Homogeneous Heterogeneous Indoor) model, assumes a uniformly mixed environment, taking into account emissions, ventilation, chemistry and deposition processes. The chemical mechanism solving the gas-phase chemistry is RACM2 (Goliff et al., 2013). Deposition is modelled as in Mendez et al. (2017). As in Finlayson-Pitts et al.

95 (2003) and Ramazan et al. (2004), the rate constants of the heterogeneous reactions are adjusted so as to obtain a reasonable match with the experimental data. Contrary to other box models (Nazaroff and Cass, 1986; Sarwar et al., 2002; Carslaw, 2007; Courtey et al., 2009; Mendez et al., 2015), this model does not assume the light to be homogeneous throughout the room. Here, two different parts are considered, one irradiated by direct light and another one illuminated indirectly. It is the first two-box model allowing to consider the evolution of light intensity of each part along the day, as well as the volumes they occupy (LCE,

100 in prep).

First, this paper gives a detailed description of the H^2I model. The input data and the tunable parameters of the model are then described. These parameters are calibrated by comparing the simulation results to the concentration profiles, which were acquired in Martigues. For each experiment, the set of parameters leading to the best simulation, called reference simulation, is given. Each of the parameters is then varied so as to estimate their sensitivity, and identifying the most impacting processes.

105 Finally a surface saturation limit is implemented to test the model in high NO_2 conditions.

2 Presentation of the H^2I (Homogeneous Heterogenous Indoor) model

2.1 Master equation

The room is divided into two volumes, a volume illuminated by the light of the sun, and a darker one illuminated by indirect light. As these lights have different intensities, the magnitudes of the photolytic reactions occurring inside these volumes are

110 different, leading to different concentrations in each volume. m_i^j [μg] is the mass of species i in the box j, with $j = \{L, S\}$, L denoting the box illuminated by direct light and S denoting the shaded box. The evolution of m_i^j with time is given by the classical box model equation (e.g. Sarwar et al. (2002); Carslaw (2007)) complemented by a box exchange term (Furtaw Jr. et al., 1996) :

$$\frac{dm_i^j}{dt} = k_{AER} f m_i^{Out} - k_{AER} m_i^j - k_{DEP,i}^j m_i^j + k_{BOX}^j \Delta_j m_i + \sum_p Q_{p,i}^j + \sum_q R_{i,q}^j \qquad (1)$$

115 where t is the time [s], k_{AER} is the air exchange rate between the room and its outside [s^{-1}], including the rest of the building, f is the outdoor-to-indoor filtration factor [-], *i.e.* the fraction of air exchange with outdoor, m_i^{Out} is the outdoor mass of species i introduced in box j [μg], $k_{DEP,i}^j$ is the deposition rate of species i [s^{-1}], $Q_{p,i}$ is the emission rate of source p [μg.s^{-1}], k_{BOX}

is the air exchange rate between the boxes [s^{-1}], $\Delta_j m_i$ is the corresponding mass transfer [μg] and $R_{i,q}^j$ is the mass reaction rate between species i and species q [μg.s^{-1}].

120   By denoting V_{box}^j the volume of the box j [m^3], the mass transfer from box L to box S is expressed as

$$\Delta_L m_i = -m_i^L + \frac{V_{\text{box}}^L}{V_{\text{box}}^S} m_i^S \tag{2}$$

and the mass transfer from box S to box L as

$$\Delta_S m_i = \frac{V_{\text{box}}^S}{V_{\text{box}}^L} m_i^L - m_i^S. \tag{3}$$

The evolution of the species concentrations is obtained by dividing Eq. (1) by the box volume. This yields

125    $$\frac{dC_i^j}{dt} = k_{\text{AER}} f C_i^{\text{Out}} - k_{\text{AER}} C_i^j - k_{\text{DEP},i}^j C_i^j + k_{\text{BOX}}^j \Delta_j C_i + \sum_p \frac{Q_{pi}^j}{V_{\text{box}}^j} + \sum_q \frac{R_{iq}^j}{V_{\text{box}}^j} \tag{4}$$

where $C_i^j = m_i^j / V_{\text{box}}^j$ is the indoor concentration of species i in volume j [μg.m^{-3}], C_i^{Out} is the outdoor concentration of species i [μg.m^{-3}] and $\Delta_j C_i$ is the concentration variation caused by the gas transfers between boxes [μg.m^{-3}], given by

$$\Delta_L C_i = -C_i^L + C_i^S,$$
$$\Delta_S C_i = C_i^L - C_i^S. \tag{5}$$

On the right-hand side of Eq. (4), the first term is the intake of species coming from outdoors. The second term is the
130   concentration loss due to the leakages toward outdoors, but also toward the other rooms of the building. The third term is deposition. The fourth term brings in the mixing between the two volumes. The fifth term represents the indoor sources that release species i and the last term is the contribution of the reactions involving species i.

The two types of sources encountered in these experiments are the emissions of the paint boards placed on the walls, $Q_{\text{paint},i}$, and the emissions of the building itself, $Q_{\text{room},i}$. The room emissions in the box j can be written as

135    $$Q_{\text{room},i}^j = Q_{\text{room},i} \frac{V_{\text{box}}^j}{V_{\text{room}}}. \tag{6}$$

The paint emissions are derived from their surface emission rates :

$$Q_{\text{paint},i}^j = E_{\text{paint},i}^j S_{\text{paint}}^j \tag{7}$$

where $E_{\text{paint},i}$ are the paint surface emission rates obtained experimentally [μg.m^{-2}.s^{-1}] and S_{paint}^j is the surface of paint in the box j [m^{-2}]. In the box illuminated by direct light, Eq. (4) thus gives

140    $$\frac{dC_i^L}{dt} = k_{\text{AER}}(f C_i^{\text{Out}} - C_i^L) - k_{\text{DEP},i}^L C_i^L + k_{\text{BOX}}^L(-C_i^L + C_i^S) + \frac{Q_{\text{room},i}}{V_{\text{room}}} + \frac{E_{\text{paint},i}^L S_{\text{paint},i}^L}{V_{\text{box}}^L} + \sum_q \frac{R_{iq}^j}{V_{\text{box}}^L} \tag{8}$$

and in the shaded box, Eq. (4) gives

$$\frac{dC_i^S}{dt} = k_{\text{AER}}(f C_i^{\text{Out}} - C_i^S) - k_{\text{DEP},i}^S C_i^S + k_{\text{BOX}}^S(C_i^L - C_i^S) + \frac{Q_{\text{room},i}}{V_{\text{room}}} + \frac{E_{\text{paint},i}^S S_{\text{paint},i}^S}{V_{\text{box}}^S} + \sum_q \frac{R_{iq}^j}{V_{\text{box}}^S}. \tag{9}$$

2.2 Boxes evolution and exchanges between the boxes

We denote V_{box}^L and V_{box}^S the volumes of the sunlit and shaded boxes. Accordingly, the total surface of the room S_{room} is split
145 into two parts, S_{box}^L and S_{box}^S. Their evolutions along the day are constrained by the relationships

$$
\begin{aligned}
V_{\text{room}} &= V_{\text{box}}^L + V_{\text{box}}^S \\
S_{\text{room}} &= S_{\text{box}}^L + S_{\text{box}}^S
\end{aligned}
\tag{10}
$$

where $V_{\text{room}} = 32.8\,\text{m}^3$ is the total volume of the room and $S_{\text{room}} = 62.7\,\text{m}^2$.

Hourly values of V_{box}^L and S_{box}^L were estimated by modelling the solar flux in the room (see article LCE (in prep)). The
position of the sun and extrapolation of its beams from the windows were assessed with the Revit 2018 software; the irradiated
150 surface and beams volume were then calculated by vertical and horizontal projections of the indoor solar flux using Autocad
2016 (see www.autodesk.fr for both softwares). The evolution of V_{box}^L and S_{box}^L as a function of time t_h [h] is inferred from
these values by fitting a Gaussian law (Fig. 1) :

$$
V_{\text{box}}^L(t_h) = \frac{A_v}{\sigma_v \sqrt{2\pi}} e^{-\frac{(t_h - \mu_v)^2}{2\sigma_v^2}}
\tag{11}
$$

with $A_v = 36.505\,\text{m}^3.\text{h}$, $\sigma_v = 2.154\,\text{h}$ and $\mu_v = 11.199\,\text{h}$,

155 $$
S_{\text{box}}^L(t_h) = \frac{A_b}{\sigma_b \sqrt{2\pi}} e^{-\frac{(t_h - \mu_b)^2}{2\sigma_b^2}}
\tag{12}
$$

with $A_b = 36.958\,\text{m}^2.\text{h}$, $\sigma_b = 2.1950\,\text{h}$ and $\mu_b = 11.555\,\text{h}$. V_{box}^S and S_{box}^S are deduced from V_{box}^L and S_{box}^L using Eq. (10).

S_{box}^L and S_{box}^S divide the total solid surface of the experimental room, including walls, window, floor and ceiling. The
complement of S_{box}^L to obtain the surface of the volume V_{box}^L is the same as the complement of S_{box}^S, necessary to obtain
the surface of V_{box}^S. This complement is the surface allowing gas transfer between the boxes, and is denoted S_{gas}. This latter
160 was estimated with the same method as the one used for V_{box}^L and S_{box}^L (LCE, in prep), giving (Fig. 1)

$$
S_{\text{gas}}(t_h) = \frac{A_g}{\sigma_g \sqrt{2\pi}} e^{-\frac{(t_h - \mu_g)^2}{2\sigma_g^2}}
\tag{13}
$$

where $A_g = 120.04\,\text{m}^2.\text{h}$, $\sigma_g = 2.4683\,\text{h}$ and $\mu_g = 11.154\,\text{h}$.

The variation of mass within the boxes due to the air mixing is proportional to the surface S_{gas}. This proportionality is
expressed by the air exchange constant k_{BOX}, defined as (Furtaw Jr. et al., 1996)

165 $$
k_{\text{BOX}}^j = u_{\text{inf}} \frac{S_{\text{gas}}}{V_{\text{box}}^j}
\tag{14}
$$

where u_{inf} is the average speed of air in the room. This velocity was estimated based on a tracer injection experiment and
numerical tests (see sections 3.2 and 5.1.1).

2.3 Chemical mechanism

Numerical simulations cannot afford the computation of the millions of reactions occurring in real atmospheres. Approxima-
tions are required to reduce this complexity and alleviate computational efforts. Modellers can opt for different types of kinetic
chemical mechanisms, depending on the targeted accuracy. In particular, the lumped-species approach allows to make use of
a reduced number of compounds, each compound representing several species having similar properties (Gery et al., 1989;
Stockwell et al., 1990; Carter, 2010; Yarwood et al., 2005; Goliff et al., 2013), such as reactivity with OH or carbon bounds.
A given species can be represented by a single model compound, or by the combination of several model compounds. Mendez
et al. (2015) compared the concentrations they obtained with such kind of lumped-species model, SAPRC-07 (Carter, 2010),
to the concentrations Carslaw (2007) simulated with the detailed chemistry model MCM, and concluded that their overall
behaviors were consistent, with respect to the O_3, NOx (NO + NO_2) and HOx (HO + HO_2) variations. Considering that the
general dynamics of homogeneous indoor chemistry can be reproduced by semi-explicit models initially developed for out-
door atmospheres, RACM2 (Goliff et al., 2013), which is also a lumped-species based model, is used in this paper to solve the
chemical reactivity.

To introduce the surface chemistry highlighted by laboratory studies but hardly present in current indoor models, the RACM2
scheme is modified so as to take into account the heterogenous reactions listed in Tab. 1. The resulting modified version of the
RACM2 scheme comprises 117 species and 389 reactions among which 34 are photolytic and 38 heterogeneous. To investigate
further the reactions highlighted in the introduction, some surface species are introduced, namely $NO_{(ad)}$, $NO_{2\,(ad)}$, $HONO_{(ad)}$
and $HNO_{3\,(ad)}$. These species can either sorb, desorb or react together. $HNO_{3\,(ad)}$ is not allowed to desorb, to account for the ex-
perimental observation that the NO_2 hydrolysis never yields gaseous HNO_3 (Finlayson-Pitts et al., 2003). The kinetic constants
of desorption and surface reactions are uncertain, and thus considered as tunable parameters. Adsorption and decomposition
reactions are modelled by combining transport to the boundary layer and surface adhesion (Mendez et al., 2015), as now
detailed.

2.4 Deposition and surface reactivity

This section details the computation of the kinetic constants of the adsorption and decomposition reactions. The local deposition
rate $k_{\mathrm{DEP},i}^{j}$ is modelled as the equivalent of two resistances in parallel, one corresponding to the transport-limited deposition
rate $k_{\mathrm{tran},i}^{j}$ and one corresponding to the surface adhesion rate $k_{\mathrm{react},i}^{j}$:

$$\frac{1}{k_{\mathrm{DEP},i}^{j}} = \frac{1}{k_{\mathrm{tran},i}^{j}} + \frac{1}{k_{\mathrm{react},i}^{j}}. \tag{15}$$

When $k_{\mathrm{react},i}^{j}$ is larger than $k_{\mathrm{tran},i}^{j}$ the species loss is limited by the transport to the surface boundary layer. A contrario, when
$k_{\mathrm{tran},i}^{j}$ is larger than $k_{\mathrm{react},i}^{j}$, species removal is limited by surface reactivity (Grøntoft and Raychaudhuri, 2004).

2.4.1 Transport-limited deposition rate

The rate constant $k^j_{\mathrm{tran},i}$ can be expressed as

$$k^j_{\mathrm{tran},i} = v_{\mathrm{trd},i} \frac{S^j_{\mathrm{box}}}{V^j_{\mathrm{box}}} \tag{16}$$

200 where $v_{\mathrm{trd},i}$ is the deposition velocity limited by transport. It is computed using the method of Lai and Nazaroff (2000), following the same approach as Mendez et al. (2017) to model the heterogeneous production of HONO :

$$v_{\mathrm{trd},i} = v^{ad}_{\mathrm{trd},i} u^* \tag{17}$$

where $v^{ad}_{\mathrm{trd},i}$ is a dimensionless deposition velocity whose computation is detailed below, and u^* is the friction velocity defined by

205 $$u^* = \left(\nu \left. \frac{\mathrm{d}U}{\mathrm{d}y} \right|_{y=0} \right)^{1/2} \tag{18}$$

with U the mean air speed parallel to the surface [m.s^{-1}], y the distance from the surface [m] and ν the air kinematic viscosity [m^2.s^{-1}], defined by $\nu = \eta/\rho$ with η the air dynamic viscosity [kg.m^{-1}.s^{-1}] and ρ the air volumetric mass [kg.m^{-3}]. Considering the narrow temperature range encountered in these experiments, ρ is approximated with the ideal gas law. The viscosity η is expressed as function of temperature T [K] using the semi-empirical Sutherland relationship

210 $$\eta(T) = \eta_0 \left(\frac{T}{T_0} \right)^{3/2} \frac{T_0 + S}{T + S} \tag{19}$$

where the Sutherland's constant for air is $S = 113$ (Kaper and Ferziger, 1972), and $\eta_0 = 1.783 \times 10^{-5}$ kg.m^{-1}.s^{-1} at $T_0 = 288.15$ K.

The derivative of U is given by

$$\left. \frac{\mathrm{d}U}{\mathrm{d}y} \right|_{y=0} = \left(\frac{0.074}{\rho \nu} \right) \left(\frac{\rho u^2_{\mathrm{inf}}}{2} \right) \left(\frac{u_{\mathrm{inf}} L}{\nu} \right)^{-1/5} \tag{20}$$

215 where L is a characteristic length of the room surface, typically $L = (V_{\mathrm{room}})^{1/3}$.

As in Mendez et al. (2017), gravity is assumed to be negligible for gases, *i.e.* the dimensionless deposition velocity $v^{ad}_{\mathrm{trd},i}$ is the same for horizontal and vertical surfaces. Assuming that the molecules eddy diffusivity equals the fluid turbulent viscosity ν_t in indoor environments, Lai and Nazaroff (2000) showed that

$$\frac{1}{v^{ad}_{\mathrm{trd},i}} = \int_{r_0}^{30} \left(\frac{1}{\frac{\nu_t}{\nu} + \frac{D_i}{\nu}} \right) \mathrm{d}y^{ad} \tag{21}$$

220 where D_i is the diffusion coefficient of species i [m.s^{-1}], y^{ad} is the adimensional distance from the surface, and r_0 is the radius of the particle, taken here as zero. The ratio ν_t/ν is given by Lai and Nazaroff (2000) for several intervals of y^{ad}. The

diffusion coefficient can be estimated based on the species critical temperature T_c [K] and critical volume V_c [cm^3.mol^{-1}], following various models. Among all the models tested in the comparative study of Ravindran et al. (1979), the model of Chen and Othmer (1962) is the one that showed the best agreement with their experimental data. Considering a species i diffusing in air, this model gives

$$D_i = \frac{4.3 \times 10^{-5} \left(\frac{T}{100}\right)^{1.81} \left[(M_{air} + M_i)/(M_{air}M_i)\right]^{1/2}}{P \left(\frac{T_{c,air}T_{c,i}}{10^4}\right)^{0.1406} \left[\left(\frac{V_{c,air}}{100}\right)^{0.4} + \left(\frac{V_{c,i}}{100}\right)^{0.4}\right]^2} \tag{22}$$

where P is the ambient pressure [atm], M_i is the species molar mass and $M_{air} = 28.97$ g.mol^{-1}.

The diffusion coefficients are computed with this method for each RACM2 compound listed in Tab. 2 with the parameters used for this calculation. In this table, T_c and V_c are the critical temperature and volume of the chemical species that are considered to be representative of the RACM2 lumped-compounds. The references from which the T_c values are taken are specified. When there is no reference, T_c is computed with the method of Joback and Reid (1987). As experimental values of V_c are difficult to find for a variety of species, they are also computed with the method of Joback and Reid (1987), excepted for methanol, xylene, and butanol, whose reference provides both T_c and V_c.

2.4.2 Surface reaction rate

Surface adhesion is modelled with the rate constants $k^j_{\text{react},i}$ which are defined as

$$k^j_{\text{react},i} = \frac{\gamma_i \omega_i}{4} \frac{S^j_{\text{box}}}{V^j_{\text{box}}}, \tag{23}$$

where γ_i is the uptake coefficient [-] and ω_i the thermal velocity [m.s^{-1}] of species i. γ_i is the ratio of collisions of species i with the surface that yield reaction or simple deposition, to the total number of collisions. ω_i depends on the the temperature and can be expressed as

$$\omega_i = \sqrt{2.1171 \times 10^4 \frac{T}{M_i}}. \tag{24}$$

The uptake coefficient is characteristic of the relationship between the species and the surface itself. It has been determined experimentally with the paints used in this study for two species, NO$_2$ and xylene, meaning that uptake coefficients of other species are unknown. The deposition of organic species is out of the scope of this paper, as organic concentrations are set to the measured values here. The uptake coefficients of NO, HONO and O$_3$ are uncertain, and thus considered as tunable parameters. Since the simulated concentrations of NO$_3$, HNO$_3$, HNO$_4$ and H$_2$O$_2$ are low, they are given an infinite uptake for simplicity, so that their deposition is only controlled by transport ($k^j_{\text{DEP},i} = k^j_{\text{tran},i}$). By default, the same procedure is applied to the HO$_2$ radical, noting that the relative difference with neglecting its deposition is of the order of 14%, which is much less than the uncertainty on its measurement (Kukui et al., 2008). The deposition of the HO radical is considered as negligible compared to its consumption by reactivity (Sarwar et al., 2002).

2.4.3 Parameterization of $\gamma_{\mathrm{NO_2}}$

The uptake coefficient $\gamma_{\mathrm{NO_2}}$ was measured in various laboratory conditions by Gandolfo et al. (2015, 2017). This section details how parameterizations are inferred from these measurements and how they are used to calculate $\gamma_{\mathrm{NO_2}}$ as a fonction of ambiant conditions.

The measurements made as a function of the relative humidity, denoted H, are normalized by the measurement made at H_{ref} = 40%. This gives, using a polynomial fitting :

$$\gamma_{\mathrm{NO_2}}^{\mathrm{norm},H}(H) = \sum_{k=0}^{2} a_k H^k \tag{25}$$

where $a_0 = 0.706$, $a_1 = 1.50 \times 10^{-2}$ and $a_2 = -2.31 \times 10^{-4}$.

Considering that $\gamma_{\mathrm{NO_2}}$ varies with the $\mathrm{NO_2}$ concentration in the room, measurements were made as a function of the $\mathrm{NO_2}$ concentration in ppb, denoted N. By normalizing these measurements by the measurement made at $N_{\mathrm{ref}} = 40$ ppb, an exponential fitting gives :

$$\gamma_{\mathrm{NO_2}}^{\mathrm{norm},N}(N) = 118.06 \ \exp^{\frac{-(N+64.52)}{20.41}} + 0.61. \tag{26}$$

Measurements were also made as a function of the light intensity irradiating the surface, denoted I. The light intensity produced by the reactor covered a spectrum ranging from 340 nm to 400 nm. Because the paint photocatalytic effect reaches saturation above a certain light threshold, a function type that does not increase too much at high intensity is chosen to express $\gamma_{\mathrm{NO_2}}^{\mathrm{norm},I}$. Using the measurements normalized by the measurement made at $I_{\mathrm{ref}} = 8.5$ W.cm^{-2}, a logarithmic fitting gives :

$$\gamma_{\mathrm{NO_2}}^{\mathrm{norm},I}(I) = \ln(I + 19.63) - 2.74. \tag{27}$$

Contrary to the other measurements, the measurements made as a function of temperature were performed at $I = 20$ W.m^{-2}. By dividing the measurements as a function of I by the measurement made at $I = 20$ W.m^{-2}, a relationship similar to Eq. (27) is obtained, and denoted $\gamma_{\mathrm{NO_2}}^{\mathrm{norm},I_2}$. By multiplying the measurements as a function of temperature by $\gamma_{\mathrm{NO_2}}^{\mathrm{norm},I_2}(I_{\mathrm{ref}})$, these measurements are brought to the same conditions of irradiance as the other measurements. They are then divided by the measurement made at $T_{\mathrm{ref}} = 296$ K. Finally, a polynomial fitting gives :

$$\gamma_{\mathrm{NO_2}}^{\mathrm{norm},T}(T) = b_1 T_s(T) + b_0 \tag{28}$$

where $b_0 = -17.62$ and $b_1 = 6.25 \times 10^{-2}$ K^{-1} for the paint containing 3.5 % of $\mathrm{TiO_2}$. The values $b_0 = 1$ and $b_1 = 0$ are preferred for the reference paint, considering that the observed decreasing trend falls within the measurements uncertainty. T_s is the temperature of the surface of paint [K]. In a real room, T_s depends on a variety of factors, including location, season, orientation, ambient temperature and surface coating (Shen et al., 2011). For the simulations, T_s is set such as $T_s = T$ in the shaded box and $T_s = 1.2 \times (T - 273.15) + 273.15$ in the sunlit box.

The $\gamma_{\mathrm{NO_2}}$ at a given set of parameters H, N and T is calculated from the reference uptake coefficient $\gamma_{\mathrm{NO_2}}^{\mathrm{ref}}$ measured at T_{ref} = 296 K, $H_{\mathrm{ref}} = 40\%$, $I_{\mathrm{ref}} = 8.5$ W/m^{-2} and $N_{\mathrm{ref}} = 40$ ppb, according to

$$\gamma_{\mathrm{NO_2}}(H,N,T) = \gamma_{\mathrm{NO_2}}^{\mathrm{ref}} \gamma_{\mathrm{NO_2}}^{\mathrm{norm},N}(N) \gamma_{\mathrm{NO_2}}^{\mathrm{norm},H}(H) \gamma_{\mathrm{NO_2}}^{\mathrm{norm},T}(T). \tag{29}$$

The parameterization $\gamma_{NO_2}^{norm,I}$ is not considered in Eq. (29), given the fact that it was established based on measurements with a light spectrum ranging from 340 nm to 400 nm, and that the measurements presented in this paper were obtained with a light spectrum starting from 395 nm.

The dependence of $\gamma_{NO_2}^{ref}$ with the percentage of TiO$_2$ nanoparticles contained by the paint and the parameterizations of 285 $\gamma_{NO_2}^{norm}$ are presented in Fig. 2. $\gamma_{NO_2}^{ref}$ increases with % TiO$_2$ but the values at 0 % and 3.5 % are very close. In the simulations, $\gamma_{NO_2}^{ref} = 5 \times 10^{-6}$ is used for both paints and for the surface that is not covered by paint (floor, ceiling, rest of the walls).

2.5 Photolysis

In all of the indoor models presented in the introduction, light was assumed to have two origins, sunlight and artificial light. Using the indoor light intensity recommended for reading purposes, Sarwar et al. (2002) assumed that each light source ac-
290 counted for 50% of the total light, and combined accordingly spectral power distributions obtained from the literature to obtain the total spectral distribution. Nazaroff and Cass (1986), Mendez et al. (2015) and Carslaw (2007) computed their own outdoor photon fluxes, and applied attenuation factors to account for window filtration. Carslaw (2007) and Mendez et al. (2015) used the same indoor light fluxes as Nazaroff and Cass (1986), and started with the same attenuation factors before varying them.

Whereas light intensity is homogeneous in the direct light whatever the distance from the window, it decreases rapidly as
295 getting away from the direct sunlight (Gandolfo et al., 2016). The distribution of light intensity in the shaded volume is strongly location-specific, and thus hard to predict. However, light intensity in the shaded volume is much lower than the intensity of direct light, so the impact of the photolytic reactions occurring in the shaded volume is minor compared to those occurring in the sunlit volume. As an approximation, the photolysis constants in the shaded box are computed using a unique actinic flux which was measured close to the area illuminated by the sunlight. This model does not represent the light decrease as getting
300 away from the window, because only two boxes are considered, shaded and sunlit.

Let ζ be the indoor actinic flux [photons.cm^{-2}.s^{-1}.nm^{-1}] measured at $t = t_{ref}$. Let λ_{min} and λ_{max} be the minimum and maximum wavelengths of the light spectrum [nm]. The photolysis constants associated to this actinic flux are given by (Nazaroff and Cass, 1986) :

$$J_i^{ref} = \int\limits_{\lambda_{min}}^{\lambda_{max}} \zeta(\lambda)\kappa_i(\lambda)\phi_i(\lambda)\mathrm{d}\lambda \tag{30}$$

305 where J_i^{ref} is the photolysis constant of species i [photons.cm^{-2}.s^{-1}] at $t = t_{ref}$, κ_i the species cross section [-] and ϕ_i the species quantum yield [-]. The actinic flux used to calculate J_i^{ref} in the indirect light was measured at $t_{ref} = 11$ h (GMT) on the 27th October (Experiment 1), and the one used to calculate J_i^{ref} in the direct light was measured at $t_{ref} = 11$ h (GMT) on the 29th October (Experiment 3). The light spectrum starts at $\lambda_{min} = 390$ nm in the direct light, and $\lambda_{min} = 394$ nm in the indirect light. Both spectra end at 660 nm.

310 To account for the evolution of the photolytic constants with day time, a parameterization is inferred from the HONO, NO$_2$, HCHO, H$_2$O$_2$ and NO$_3$ photolysis rates measured by a spectroradiometer in the direct light on the 30th October, with windows

that did not cut UV rays (Fig. 3) :

$$J_i(\theta) = A_i \exp^{\frac{-(\theta-C)}{B}},\tag{31}$$

where θ is the zenith angle and J_i is the photolysis constant of species i as a function of θ. The evolution of θ with day hour is
presented in Fig. 4. The curves fitting the J_i rates measured in the morning and those fitting the ones measured in the afternoon
are superimposed in Fig. 3, indicating no hysteresis. For each compound, the values of B and C are very close, with an average
of $B = 10.77$ and $C = 50.03$. For a given compound, the prefactor A is given by

$$A_i = J_i^{\mathrm{ref}} \exp^{\frac{\theta_{\mathrm{ref}} - C}{B}},\tag{32}$$

where θ_{ref} is the zenith angle corresponding to t_{ref}. This yields

$$J_i(\theta) = J_i^{\mathrm{ref}} \exp^{\frac{-(\theta-\theta_{\mathrm{ref}})}{B}}.\tag{33}$$

Eq. (33) is plotted in Fig. 3 using the J_i^{ref} calculated with the ϕ and κ values available for the RACM2 chemical mechanism
(Kim et al., 2009) in the Polyphemus air-quality modelling platform. We observe a reasonable agreement between the measured
and calculated photolysis rates.

2.6 Numerical resolution

The simulations start and end at the times fixed by the user (see section 3.1). The time step Δt of the main loop of time of
the program is set to $100\,\mathrm{s}$. It corresponds to an input/output time step: at the beginning of each iteration of the main loop,
input data, such as temperature, humidity, and outdoor concentrations, are read from a file; and at the end of each iteration,
the concentrations are written to a file. Variables characterizing the environment, source and sink terms are also initialized
and updated in the main loop : box volumes and surfaces (Eqs. 10-12), box air exchanges (Eq. 14), ventilation, supply from
outdoors, and emissions.

The resolution of Eq. (4) is performed using operator splitting : the evolution of the concentrations due to emissions, air
exchanges between boxes and between the room and the outside is first solved using the explicit trapezoidal rule (ETR),
which is an explicit second order solver corresponding to a two-stage Runge-Kutta method (Ascher and Petzold, 1998). The
time step is adapted as described in Sartelet et al. (2006) : each main time step Δt of $100\,\mathrm{s}$ is decomposed in sub-time steps
δt_k determined by the ETR method, such as $\Delta t = \sum_k \delta t_k$. After each sub-time step δt_k, the third and last term of Eq. (4)
are solved together. The evolution of the concentrations due to homogeneous and heterogeneous reactions and deposition is
computed using the Rosenbrock 2 (ROS2) algorithm (Rosenbrock, 1963; Sandu et al., 1997), with time steps automatically
adapted between δt_k and δt_{k+1} by the ROS2 algorithm.

In this paper, the VOCs are assigned to their experimental values at each iteration of the main loop. By imposing the
VOCs concentrations at each main iteration, no drift is observed between experimental and calculated values, meaning that
the characteristic time of their evolution caused by chemical reactivity, sources and sinks is slower than the model time step
Δt. Note that this is not the case with more reactive species, such as NO, NO_2 and radicals, which may evolve significantly
between two iterations.

3 Input data and parameters for model evaluation

3.1 Measurements used as input and model/measurement comparisons

Three experiments were conducted with anti-UVs windows. The first one was conducted without any paint board ("naked" walls), the second one with walls covered by the reference paint, and the third one with walls covered by the 3.5% TiO_2 paint.

The room was ventilated before each experiment. The start time of the simulation is chosen so as to match with the beginning of the VOC concentrations rise caused by the windows closing. When the windows were closed, the air exchange rate k_{AER} was determined by continued analysis of an inert gaseous tracer (CO_2) injected in the room at the beginning of the experiment. For a given day, the measured k_{AER} were almost constant, which allows to run the simulations with a daily average value for each experiment. Indoor temperature and humidity were measured each ten seconds. They are involved in the computation of air viscosity, friction velocity, species diffusivities, thermal and deposition velocities, and uptake values. The durations of the experiments, average ventilation rates, as well as the minimum and maximum temperatures and humidities recorded are summarized in Tab. 3.

Outdoor concentrations, used as model input, are estimated by linear interpolation of outdoor measurements. VOCs were measured with a PTR-MS-ToF (Proton Transfer Reaction - Mass Spectrometer - Time of Flight) equipped with a motorized valve rotating alternatively for 5 minutes outdoors and 10 minutes indoors, providing an outdoor VOC measurement each 15 minutes. The O_3 outdoor concentrations were measured at a rate of one measurement per minute. The NO and NO_2 outdoor concentrations were recorded on a quarter-hourly basis by the regional air-quality network AtmoSud at a station located about 1.5 km away and for which the NOx concentrations are expected to be representative of the concentrations close to the building. Outdoor HONO, HO and HO_2 were not measured. They are thus fixed at a constant and realistic value of 20 ppt for HONO, 10^6 molecules per cubic centimeter (molecules.cm^{-3}) for OH and 10^8 molecules.cm^{-3} for HO_2 (Holland et al., 2003).

Due to the PTR-ToF-MS valve rotations, an indoor VOC measurement each 15 minutes was performed with a shift of 5/10 minutes with the previous/subsequent outdoor VOC measurement. Indoor NOx were measured by chimiluminescence, HONO using a LOPAP (LOng Path Absorption Photometer), O_3 by spectrophotometry and radical species using a CIMS (Chemical Ionisation Mass Spectrometer). All of the instruments were placed in a separate room, apart from the CIMS which could not be moved away. The presence of instruments in the experiments room would have increased the surface available for heterogeneous reactivity in a hardly quantifiable way, thus introducing uncertainty. O_3 was captured at the center of the room, at a rate of one measurement per minute. NOx were measured each second and HONO each 15 seconds. The modelled O_3, HONO, NOx and radicals are compared to these experimental records. The sources of these species are infiltration from outdoors and chemical reactivity, so no emission rate is considered for them.

3.2 Model parameters

The inorganic species measurements are considered as a benchmark to estimate the model undetermined parameters. These parameters are the building filtration factor f, the kinetic constants of the surface and desorption reactions (see Tab. 1), the

uptake coefficients of O_3, NO and HONO, the initial concentrations of the surface species $NO_{(ad)}$, $NO_{2(ad)}$, $HONO_{(ad)}$ and $HNO_{3(ad)}$ and, to a lesser extent, the speed of air in the room u_{inf}.

The speed of air in the room is assessed by measuring the homogenization time of a tracer gas injection. A styrene injection allowed to estimate that this speed could range between 0.05 and $0.4 \, \text{m.s}^{-1}$. Furtaw Jr. et al. (1996) and references therein

380   suggest the same admissible bounds for this parameter, with a value of $0.15 \, \text{m.s}^{-1}$ identified as reference for indoor comfort conditions (McQuiston et al., 2004). In the experiments of this paper, two fans were placed on both sides of the room, providing an active air mixing, and thus a u_{inf} value likely exceeding $0.15 \, \text{m.s}^{-1}$.

The building filtration factor controls the pollutants fluxes from outdoor, and is completely undetermined. According to Sarwar et al. (2002), its value ranges between 0.10 (airtight building) and 0.90 (permeable building). In the absence of mea-

385   surement, it is omitted or taken as unity in most models (Sarwar et al., 2002; Carslaw, 2007; Mendez et al., 2015).

Among the surface species introduced in this model, NO_2 is the only one whose uptake value was determined experimentally, the other ones are adjusted by the user. The value of γ_{NO} is expected to be low, given that all the models consider a zero deposition velocity for NO, following Nazaroff and Cass (1986). The uptake coefficients provided for NO, HONO and O_3 are supposed to be the uptake values at $T_{ref} = 296$ K, $H_{ref} = 40\%$, $I_{ref} = 8.5 \, \text{W/m}^{-2}$, at a concentration of 40 ppb. Their variations

390   are parameterized with the same relationships as the ones obtained for NO_2 (see section 2.4.3).

According to Ramazan et al. (2004), water competes with $HONO_{(ad)}$ for surface sites, and displaces $HONO_{(ad)}$ toward gas phase as the surface water vapor increases. The higher the water vapor, the more $HONO_{(ad)}$ desorbs. On the opposite, the lower the water vapor, the more $HONO_{(ad)}$ is available to react with other sorbed species such as NO. In this study, it is assumed that the same holds for the other adsorbed compounds. As no information on the surface water concentration is available, the

395   desorption reactions are parameterized as a function of the room humidity. The desorption kinetic constants are defined as

$$k_{i,(ad)} = \alpha_i k_{H,i} n_{H_2O} \qquad (34)$$

where n_{H_2O} is the number of water molecules in the room computed from the water mass fraction (absolute humidity), $k_{H,i}$ is the Henry's Law constant of compound i [bar.mol.kg^{-1}] and α_i is a tunable variable [kg.bar^{-1}.mol^{-1}.s^{-1}.molecules^{-1}]. The value of $k_{H,i}$ characterizes the compound affinity for water. The temperature range of these experiments (see Tab. 3) is consid-

400   ered as sufficiently narrow to neglect the dependence of $k_{H,i}$ on temperature. At $T = 298.15$ K, $k_{H, NO} = 0.0019$ bar.mol.kg^{-1}, $k_{H, NO_2} = 0.012$ bar.mol.kg^{-1} and $k_{H, HONO} = 49$ bar.mol.kg^{-1} (Linstrom and Mallard). For simplicity, in the rest of this paper, we will denote $k'_{i,(ad)} = \alpha_i k_{H,i}$.

Another element that can be considered as uncertain is the stoichiometry of the NO_2 hydrolysis reaction. Generally, it is assumed that $HONO_{(ad)}$ and $HNO_{3(ad)}$ are formed with equal yields, but to date, and to the author's knowledge, no experimental

405   validation of this production ratio is available. By denoting $NO_{2(ad)} \rightarrow \beta_{HNO_3} HNO_{3(ad)} + \beta_{HONO} HONO_{(ad)}$, variations of β_{HNO_3} and β_{HONO} will be considered, with the constraint that $\beta_{HNO_3} + \beta_{HONO} = 1$, to assure nitrogen conservation.

3.3 Initial conditions

According to Nazaroff and Cass (1986), simulations can be sensitive to changes in initial conditions over a characteristic time which can be considered as proportional to the inverse of the air exchange rate. When the period simulated extends over
410 several days (Sarwar et al., 2002; Carslaw, 2007; Courtey et al., 2009), the influence of initial conditions can be neglected. In the present study, the air renewal time (k_{AER}^{-1}), *i.e.* the minimum time needed to break free from the initial conditions, represents about the half of the simulated periods, thus requiring to set the initial concentrations carefully. The RACM2 organic and inorganic compounds concentrations are initialized using the concentrations measured at the start time of the experiments, summarized in Tab. 4. However, this is not sufficient to initiate the radicals chemistry which is influenced by a variety of
415 species, including VOCs that were not measured because unidentifiable, or under the detection limit of the PTR-MS-ToF. Without proper initialization, the modelled radicals concentrations fall well below the measured ones immediately after the start of the simulation, which damages the overall chemistry and thus the comparison between model and experiments.

   To assess the initial concentrations of the species that were not detected, a simulation is run while forcing the organic and inorganic compounds to follow their measured values, for about half an hour of simulated time. The radical species cannot be
420 fixed to their experimental records, because too reactive. The time at which the simulation is stopped is denoted t_a. Then, a new simulation is launched by assigning the concentrations obtained at time t_a to the compounds that were not measured; the other ones are again initiated using the concentrations measured at the start time of the experiments, reported in Tab. 4. With these new initial conditions, the simulated OH and HO_2 initial concentrations are higher than in the previous simulation. The same procedure is repeated until that the initial HO_2 concentration reaches the same concentration as the one measured at the
425 start of the experiment, represented by the horizontal dashed line in Fig. 5.

   The simulations performed by initializing only the compounds that were quantified experimentally are labelled as "without radical initialization". The simulations performed by initializing all the species, following the procedure explained above, are labelled as "full initialization". Fig. 5 shows the radical concentrations in the sunlit box; the radicals in the shaded box are not presented, because both profiles are very similar, and the magnitude of the shift between the two curves is negligible (see
430 section 4) compared to the differences caused by the variations in initialization. The "full initialization" completely modifies the HO_2 profile, thus impacting NO and HONO, as well as the first parts of the OH and NO_2 profiles. In particular, the variations of the NOx profiles are altered in such a way that the correspondence between model and experiments is at stake without inititialization.

   It is clear that all the compounds do not contribute equally to the radical chemistry. Namely, the initialization of compound
435 PPN (PeroxylPropionyl Nitrate) allows to bridge about half of the gap between the simulations "without radical initialization" and the simulations with "full initialization". Interestingly, albeit considered as an important sink for OH (Weschler and Shields, 1996; Carslaw, 2007), the initialization of CO does not influence the HOx concentrations. Among the 68 RACM2 compounds that were not detected during the experiments but for which the model predicts a non-zero concentration, only 6 need to be initialized to get proper radical chemistry. These are PAN (Peroxyacetyl nitrate and higher saturated PANs), MGLY
440 (Methylglyoxal and other alpha-carbonyl aldehydes) DCB1, DCB2 and DCB3 (Unsaturated dicarbonyls), and PPN. The ini-

tialization of these compounds in addition the species measured experimentally provides the same effect on HO and HO_2 as the "full initialization".

It can be inferred from this section that a careful assessment of the initial concentrations, including for compounds that were not experimentally detected, is mandatory for such type of study.

445   **4   Reference simulations**

The parameters presented in section 3.2 are calibrated to reach the best correspondence between experimental data and simulations as possible. The filtration factor f varies between experiments depending on wind conditions. The speed of air and the stoichiometry of the NO_2 heterogeneous hydrolysis do not vary between experiments. However, the values of the surface kinetic reaction rates, desorption rates and uptake coefficients may vary between experiments, because of differences in wall

450 covering. Therefore, the parameters are first adjusted for each experiment independently. This set of optimized parameters is denoted "Set 1". To determine parameter values usable in a wide range of conditions, the parameters are then varied to use the same values of surface kinetic reaction rates k_S for all experiments, but letting the desorption rates $k'_{i,\,(ad)}$ vary with experiment. This leads to the set of parameters "Set 2". Finally, the set of parameters "Set 3" corresponds to parameters adjusted to use the same values for all experiments. Note that in the first experiment, the desorption constant $k'_{NO\,(ad)}$ still requires a lower value

455 than the common one. In the rest of this paper, "reference simulations" will denote the simulations obtained with the "Set 3" parameter values, while "optimized simulations" will denote the simulations obtained with the "Set 1" parameter values. All the parameter values are listed in Tab. 5.

Figs. 6, 7 and 8 present the three sets of simulations for the three experiments. In these graphs, the solid lines denote the concentrations simulated in the sunlit box, the dashed lines the concentrations in the shaded box. These two curves are identical,

460 except for the radicals, whose averaged concentrations in the shaded and sunlit volumes have a discrepancy of 5%, 7% and 3% in Experiment 1, 2 and 3 respectively. These differences are moderate, and indicate that the radical reactivity is a little more rapid than the air exchange between the sunlit and the shaded volumes. The NO, NO_2 and NOx outlying dots observed at around 10h20 and 12h10 for Experiment 1, and 12h45 and 14h20 for Experiment 3, are sporadic outdoor measurements, and are thus not simulated by the model. During Experiment 1, an artificial NO_2 injection of about 56 ppb (including a few ppb of NO)

465 was performed at 13h30. The simulated NO and HONO outbreaks generated by this NO_2 injection exceed the concentrations measured experimentally; they arise from surface chemistry and cannot be cancelled out by changing the parameters without damaging the simulated profiles before the injection.

The similarity between simulations and experiments is quantified by computing, for the four modelled inorganic compounds, the relative error between the average measured and simulated concentrations, the Root-Mean-Square Error (RMSE), the

470 Mean Normalized Gross Error (MNGE) and the Mean Normalized Bias Error (MNBE), as presented in Tab. 6. For the first experiment, these indicators are computed over the period preceeding the NO_2 injection only.

The NOx concentration is quite well modelled in Experiments 2 and 3, with a MNGE of 4-6%. For NO_2, the MNGE is about 22% in Experiment 2 while it reaches about 28% in Experiment 3. Regarding NO, the MNGE is about 17% in Experiment 2,

and 35% in Experiment 3. In Experiment 1, the NOx concentrations are systematically underestimated, with an MNBE of -64%
475 in the first part of the simulation. In the second part, the NO_2 decay following the NO_2 injection is quite well replicated using
the optimized parameters. For all experiments and all sets of parameters, O_3 is underestimated with a relative error ranging
between 50% and 60%. HONO exhibits excellent statistics for Set 1 and Set 2, with an MNGE of 1% to 3.5% in the three
experiments. Yet, using the common parameters (Set 3), HONO is underestimated in Experiment 2 (-8% MNBE), and strongly
overestimated in Experiments 1 and 3 (94% and 78% MNBE respectively).

480 By comparing the simulations by sets of parameters, we can observe that for Experiments 2 and 3, the Set 1 and Set 2
parameters lead to very similar concentrations, whereas the use of common values for desorption constants (Set 3) increases
the error on HONO. The Set 1 results stands as the best correspondence that can be achieved. In these experiments, the
discrepancy between model and measurements observed using common parameters (Set 3) can be cancelled out by varying the
NO and HONO desorption constants (Set 2). In the first experiment, the NOx curves are identical for Set 2 and Set 3. They
485 differ from the Set 1 curves because in that case, the parameters were optimized to replicate the NO_2 decay and mitigate the
NO release following the injection.

The modelled OH concentrations are of the same order as the measured ones. The HO_2 concentrations are very similar, or
overestimated by a factor of 4 at most (Experiment 1), which is quite reasonable considering the uncertainty associated to such
species measurement (Kukui et al., 2008). In this model, radicals are controlled by homogenous chemistry, which derives from
490 the fixed VOCs concentrations and from the modelling of inorganic compounds.

It can be concluded from this section that by combining homogeneous and heterogenous reactivity, the $H^2 I$ model is able
to replicate the inorganic and radical chemistry. The model parameters which could not be determined experimentally were
treated as tunable parameters. The model yields satisfying results using the same parameter values for all experiments (Set 3),
apart from the NO profile in Expriment 1, where a lower $k'_{NO(ad)}$ is needed. The model results can be improved up to the best
495 achievable results (Set 1), by merely varying the NO and HONO desorption rates (Set 2).

5 Sensitivity study

The purpose of this section is to investigate the relative influence of the model parameters. As radicals react too rapidly
to be influenced by surface chemistry, and because organic concentrations are set to the measured values, a correct radical
modelling is expected to flow from the correct modelling of inorganic species. This section thus focuses on how surface
500 reactions determine the inorganic chemistry, as a key step toward a comprehensive IAQ modelling. As Experiment 1 is a
particular case (NO_2 injection), only Experiments 2 and 3 are considered for these tests. When a parameter is varied, the
simulated results are presented for one experiment only, as the conclusions are identical for both experiments. Each tunable
parameter is investigated independently. The parameters which are not varied are given the values as the optimized parameters
(Set 1) listed in Tab. 5.
505 The initial concentrations of the gas-phase species are determined using the procedure described in section 3.3 and are
summarized in Tab. 4. The sorbed species $NO_{(ad)}$, $NO_{2(ad)}$, $HONO_{(ad)}$ and $HNO_{3(ad)}$ do not undergo the same processes as the

gas-phase species. Their evolution is driven by chemical reactivity only. Since box exchange is disabled for these species, these species profiles in the shaded and sunlit volumes are well distinct, as shown by all the figures presented in this section. At the start of the simulations, the concentrations of these species rapidly converge to the values determined by surface chemistry.

510   Proper sorbed species initial concentrations are thus easy to set, after running a couple of simulations. For a given experiment, the initial concentrations remain unchanged whatever the parameter investigated.

5.1   Filtration factor and speed of air

Indoor chemistry is influenced by the filtration factor and the speed of air, which are parameters characteristic of the environment. The filtration factor controls the input flux of outdoor pollutants, while the speed of air governs deposition. This section

515   aims at assessing to what extent these parameters affect the overall inorganic concentrations.

5.1.1   Speed of air

The gas-phase and adsorbed inorganic compounds simulated with a speed of air u_{inf} ranging from $0.06\,\mathrm{m.s^{-1}}$ to $0.30\,\mathrm{m.s^{-1}}$ are presented in Fig. 9. This range of variations corresponds to the range of expected values described in section 3.2. The modelled NO_2 and O_3 concentrations decrease with increasing u_{inf} while the modelled NO and HONO concentrations increase

520   with increasing u_{inf}. These opposite behaviours derive from the type of the source and processes contributing to these species concentrations at most. It can be easily inferred from Eqs. (16-20) that the larger u_{inf}, the larger the deposition on surfaces. When u_{inf} is increased, the O_3 surface removal increases. As the main source of O_3 is transport from outdoor (Weschler and Shields, 1996), this loss of O_3 is not counterbalanced by another source, which results in a decrease of O_3 with increasing u_{inf}. A contrario, HONO is mainly produced by heterogeneous processes which are predominant indoors. The increase of u_{inf} en-

525   hances the NO_2 deposition, and thus the HONO production by the NO_2 hydrolysis on surfaces. Indoor NOx concentrations are influenced by both outdoor concentrations and surface chemistry (Weschler et al., 1994). In these experiments, variations with u_{inf} indicate that the main NO_2 source is outdoor infiltration whereas NO is mainly produced by heterogeneous processes. The value retained for u_{inf} is $0.24\,\mathrm{m.s^{-1}}$, considering it is large enough to achieve an effective deposition and stimulate secondary chemistry, while fulfilling the criterions presented in section 3.2. As this value is the result of controlled air mixing by fans, it

530   is kept unchanged from one experiment to the other.

5.1.2   Filtration factor

Contrary to u_{inf}, increasing f leads to an increase of NO_2 and O_3, but also of NO and HONO (see Fig. 10). It must be underlined that increasing f increases the intake of outdoor pollutants, but not the air exchange rate which remains unchanged. Increasing the fraction of air exchange with outdoor increases the concentration of outdoor pollutants like O_3 and NO_2. In turn, the

535   increased NO_2 concentration fosters the secondary production of HONO and NO. For these experiments, an average value of 0.30 appears appropriate to match the overall amount of NOx, and by extension the amount of HONO. As mentioned in section 4, differences between experiments can be caused by variations in outdoor wind conditions.

5.2 NO_2 heterogeneous hydrolysis : $NO_{2\,(ad)} \rightarrow 0.5\ HNO_{3(ad)} + 0.5\ HONO_{(ad)}$

The influence of the NO_2 heterogeneous hydrolysis is now investigated, by varying its stoichiometry and kinetic rate.

5.2.1 Stoichiometry

As introduced in section 3.2, the stoichiometry of the NO_2 hydrolysis reaction is uncertain. Fig. 11 presents the evolution of the inorganic concentrations with different yields β_{HNO_3} and β_{HONO}. Because HONO concentrations are underestimated when $\beta_{HNO_3} = \beta_{HONO} = 0.5$, the ratio $\beta_{HNO_3}/\beta_{HONO}$ is kept < 1 so that $HONO_{(ad)}$ is always more produced than $HNO_{3(ad)}$. When $\beta_{HNO_3}/\beta_{HONO}$ tends to one, the production of $HONO_{(ad)}$ and $HNO_{3(ad)}$ by the NO_2 hydrolysis gets balanced, which favours the NO production by reaction S2. As NO increases, NO_2 increases by equilibration through homogeneous chemistry. When the ratio $\beta_{HNO_3}/\beta_{HONO}$ tends to one, less $HONO_{(ad)}$ is available for desorption, and less gas-phase HONO is released. Conversely, when the ratio $\beta_{HNO_3}/\beta_{HONO}$ is decreased, the enhanced $HONO_{(ad)}$ production fosters the HONO desorption, leading to higher HONO gas-phase concentration. It is noteworthy that very small variations of $\beta_{HNO_3}/\beta_{HONO}$ generates significant variations in NOx, and particularly HONO. Note that O_3 is mainly controlled by transport from outdoor, and is thus not affected by these parameters. The values $\beta_{HNO_3} = 0.47$ and $\beta_{HONO} = 0.53$ allow to match a consistent HONO production without differing too much from the classical stoichiometry assumed for this reaction. They are kept unchanged from one experiment to the other.

5.2.2 Surface NO_2 conversion

NO_2 is adsorbed on surfaces at a rate which is determined by the transport velocity toward surfaces, and by the NO_2 uptake of surfaces. Once NO_2 is adsorbed, it is converted, in the presence of water, to form HONO and HNO_3, at a kinetic rate k_{S1} which is highly uncertain. The larger k_{S1}, the more rapid the conversion and the larger the HONO production. The same holds for NO which is produced by secondary reaction of $HONO_{(ad)}$ with $HNO_{3(ad)}$. In turn, the NO increase enhances NO_2 by homogeneous reactivity, thus providing new NO_2 available for adsorption. However, Fig. 12 shows that HONO concentrations do not vary much when k_{S1} is increased above a threshold value of $0.003\,\mathrm{s}^{-1}$. As k_{S1} is increased above this value, the $NO_{2(ad)}$ concentration tends to zero. When k_{S1} is decreased, the $NO_{2(ad)}$ hydrolysis is slowed down, which decreases the $HONO_{(ad)}$ reservoir and thus curb the NOy (NOx + HONO) heterogeneous production. The sensitivity of this parameter is large. The threshold value $k_{S1} = 0.003\,\mathrm{s}^{-1}$ is retained, as it maximizes the $NO_{2(ad)}$ conversion.

5.3 NO secondary formation

According to section 5.1.1, NO is mainly produced by secondary chemistry in these experiments. In this section, the importance of two reactions forming $NO_{(ad)}$ is studied.

5.3.1 $HONO_{(ad)} + HNO_{3(ad)} \rightarrow 2\ NO_{(ad)}$

First, $NO_{(ad)}$ can be produced by the reaction of $HONO_{(ad)}$ with $HNO_{3(ad)}$, at a kinetic rate k_{S2}. Fig. 13 shows that increasing k_{S2} enhances the formation of $NO_{(ad)}$, and thus its release to the gas-phase. As less $HONO_{(ad)}$ is available, the gas-phase HONO

concentration is lowered. A contrario, if k_{S2} is lowered, the reaction of $HONO_{(ad)}$ with $HNO_{3(ad)}$ gets slow compared to the desorption of $HONO_{(ad)}$, and most of the $HONO_{(ad)}$ is released in the gas phase. In turn, the $NO_{(ad)}$ production gets too low

570   to maintain a NO release allowing to reach the measured concentrations. These results indicate that there is a competition between the desorption of $HONO_{(ad)}$ and the reaction of $HONO_{(ad)}$ with $HNO_{3(ad)}$ to consume $HONO_{(ad)}$. When calibrating k_{S2} and $k'_{HONO(ad)}$, a balance between these two reactions must be found, to obtain consistent concentration profiles for both HONO and NO. Similarly to k_{S1}, the parameter k_{S2} seems to be a very sensitive one, as it significantly affects NO, HONO, and also NO_2 through the means of NO. The value $k_{S2} = 10^{-13}\,\text{s}^{-1}$ retained for the reference simulations is a compromise

575   between the optimized values calibrated for each experiment.

5.3.2 $HONO_{(ad)} \rightarrow 0.5\,NO_{(ad)} + 0.5\,NO_{2(ad)}$

Another $NO_{(ad)}$ formation pathway is the autoionization of $HONO_{(ad)}$. The larger the kinetic constant k_{S3} of this reaction is, the larger the $HONO_{(ad)}$ conversion into $NO_{(ad)}$ and $NO_{2(ad)}$ is, and the lower the $HONO_{(ad)}$ reservoir available for desorption is. However, contrary to reaction S_2, the autoionization of $HONO_{(ad)}$ does not compete with the desorption of $HONO_{(ad)}$. It can

580   be observed in Fig. 14 that when $k_{S3} < 10^{-5}$, the effect of this reaction vanishes, meaning that the HONO concentrations are only determined by k_{S2} and $k'_{HONO(ad)}$: as discussed in the previous subsection, decreasing k_{S2} with $k_{S3} = 10^{-5}$ enhances the release of HONO and cuts off the production of $NO_{(ad)}$, showing that reaction S_2 and desorption weigh in on the depletion of $HONO_{(ad)}$ at equal level. If k_{S3} is raised above that value, the gas-phase NOx concentrations increase, but it gets more difficult to lift HONO up to the concentrations measured experimentally, indicating that k_{S3} should not be increased too much when

585   calibrating the model kinetic constants. The threshold value $k_{S3} = 10^{-5}\,\text{s}^{-1}$ is kept for this work.

5.4 NO_2 regeneration : $NO_{(ad)} + HNO_{3(ad)} \rightarrow NO_{2(ad)} + HONO_{(ad)}$

As mentioned in the introduction, $NO_{2(ad)}$ and $HONO_{(ad)}$ can be regenerated through the reaction of $NO_{(ad)}$ with $HNO_{3(ad)}$. Fig. 15 shows that the larger the kinetic constant k_{S4} of this reaction is, the lower the NO and NO_2 concentrations are, but the larger the HONO concentration is. Increasing k_{S4} promotes the consumption of $NO_{(ad)}$, thus curbing the release of NO to the

590   gas phase. The production of $HONO_{(ad)}$ is enhanced, which in turn stimulates the HONO release. The production of $NO_{2(ad)}$ is also enhanced by reaction S_4, which should increase the $NO_{2(ad)}$ reservoir. However, reaction S_1 competes with desorption in the depletion of $NO_{2(ad)}$. As reaction S_1 reduces the surplus of $NO_{2(ad)}$ produced by reaction S_4, there is no increase of the $NO_{2(ad)}$ reservoir. The release of NO_2 is not enhanced, and the gas-phase NO_2 concentration equilibrates with the decreased NO concentration. In turn, increasing k_{S4} lowers the NO_2 concentration, whereas it raises the HONO one.

595   When k_{S4} is decreased below 10^{-15}, the effect of this reaction on the inorganic concentrations vanishes, showing that like reaction S_3, reaction S_4 does not compete with another reaction, contrary to reactions S_1 and S_2. Increasing k_{S4} increases the HONO concentration, but lessens the NOx level at the same time, which is unfavourable beyond a certain threshold. This suggests that the kinetic constant k_{S4} should remain low enough to keep reaction S_4 upstage, like reaction S_3. In these simulations, the value $k_{S4} = 2 \times 10^{-15}$ allows to back the HONO production while meeting this requirement.

5.5 Desorption constants and uptake values

The desorption constants and uptake coefficients drive the exchanges between the adsorbed and the gas phases. They are now examined.

5.5.1 Nitrogen dioxide

The uptake coefficient γ_{NO_2} is the only parameter characteristic of the heterogeneous chemistry of inorganic compounds that was determined experimentally for the paint boards. This parameter is not modified in Experiments 2 and 3 where the paint boards were used. Here, the sorption dynamics of NO_2 is only modified through the desorption constant $k'_{NO_2\,(ad)}$. It can be inferred from Fig. 16 that the NO_2 concentration is not very sensitive to $k'_{NO_2\,(ad)}$, as this latter must be varied over several orders of magnitudes to observe significant changes in NO_2 concentrations, likely because the main source of NO_2 is transport from outdoor, and not secondary chemistry. Increasing $k'_{NO_2\,(ad)}$ decreases the $NO_{2(ad)}$ reservoir. As less $NO_{2(ad)}$ is available, less $HONO_{(ad)}$ is produced by reaction S_1, thus resulting in a decreased release of HONO to the the gas phase. To maintain sufficient NO_2 adsorption and large enough HONO concentration, the parameter $k'_{NO_2\,(ad)}$ should be kept low. It is set to $k'_{NO_2\,(ad)} = 10^{-22}\,\text{s}^{-1}.\text{mlc}^{-1}$ in the reference simulations.

5.5.2 Nitric oxide

To date, all the box models (Sarwar et al., 2002; Carslaw, 2007; Courtey et al., 2009; Mendez et al., 2015) assume a zero deposition velocity for NO after the values reported by Nazaroff and Cass (1986). A zero deposition velocity corresponds to an uptake coefficient close to zero, thus preventing the molecules from colliding with surfaces and getting adsorbed.

Fig. 17 investigates the sensitivity of inorganic concentrations to γ_{NO}, which is varied between $\gamma_{NO} = 10^{-8}$ and the maximum value $\gamma_{NO} = \infty$. The coefficient $\gamma_{NO} = \infty$ is obtained by assuming that all the collisions are efficient, that is $k^j_{DEP,i} = k^j_{tran,i}$. When $\gamma_{NO} = \infty$, the NO deposition is only limited by transport to the surface. Apart from the beginning of the simulations, no significant variation in NO concentration is observed between the extreme values investigated, showing that in this experiment, deposition has a negligible contribution to the gas-phase NO concentration. The first part of the simulated profile can be improved by about 10% using the lowest γ_{NO} value.

The concentration variations with desorption constant $k'_{NO\,(ad)}$ are presented in Fig. 18. When $k'_{NO\,(ad)}$ is increased, $NO_{(ad)}$ evaporates toward gas phase. A contrario, when $k'_{NO\,(ad)}$ is decreased, the release of NO is less efficient and the NO concentration decreases, leading to a decrease in NO_2 concentration. Then, since less NO_2 is available on surfaces for hydrolysis, less HONO is produced. As a result, decreasing $k'_{NO\,(ad)}$ too much levels down the three NOy compounds concentrations in the gas phase.

In turn, the parameters γ_{NO} and $k'_{NO\,(ad)}$ should be fixed so as to keep NO in gas-phase form preferentially, which corroborates the use of a very low deposition velocity, as done in the literature. In this paper, an uptake coefficient $\gamma_{NO} = 8 \times 10^{-9}$ is chosen for all the simulations. The desorption constant $k'_{NO\,(ad)}$ is set to $8 \times 10^{-21}\,\text{s}^{-1}.\text{mlc}^{-1}$ for Experiments 2 and 3, while a lower value $2 \times 10^{-22}\,\text{s}^{-1}.\text{mlc}^{-1}$ appears required to simulate Experiment 1.

5.5.3 Nitrous acid

The adsorption/desorption dynamics of HONO is investigated by varying the uptake coefficient γ_{HONO} (Fig. 19) and the desorption constant $k'_{\text{HONO (ad)}}$ (Fig. 20). Contrary to NO, small variations of uptake coefficient and desorption constant make the HONO concentration vary a lot. HONO is not brought by transport from outdoor and is only produced by secondary chemistry,

635   which justifies the critical importance of these parameters controlling the transfers between the homogeneous gas-phase and surfaces. Increasing γ_{HONO} leads to increase the $\text{HONO}_{\text{(ad)}}$ reservoir and therefore to decrease the gas-phase HONO. When γ_{HONO} tends to zero, the gas-phase HONO concentration is determined by the desorption constant $k'_{\text{HONO (ad)}}$ only. As the HONO concentration is sensitive to both γ_{HONO} and $k'_{\text{HONO (ad)}}$, a balance between these parameters must be found. An increase in γ_{HONO} can compensate an increase in $k'_{\text{HONO (ad)}}$, and reciprocally, a decrease in γ_{HONO} must be associated with a decrease

640   in $k'_{\text{HONO (ad)}}$. Several choices (large γ_{HONO} and $k'_{\text{HONO (ad)}}$ *vs.* low γ_{HONO} and $k'_{\text{HONO (ad)}}$) allow to simulate the HONO concentration correctly. However, the time variations of the HONO concentration may behave differently depending on the chosen set of parameters. In this example, if both γ_{HONO} and $k'_{\text{HONO (ad)}}$ are large, the HONO concentration tends to bend at the end of the simulation, whereas a monotonous increase is observed in the experiment. This suggests that low values of γ_{HONO} and $k'_{\text{HONO (ad)}}$ are better suited. The values $\gamma_{\text{HONO}} = 2 \times 10^{-8}$ and $k'_{\text{HONO (ad)}} = 5 \times 10^{-22}\,\text{s}^{-1}.\text{mlc}^{-1}$ are retained for the reference

645   simulations.

Finally, while significant variations of HONO concentrations are observed, changes in NO and NO_2 are imperceptible, thus showing the poor correlation between HONO and NOx concentrations in these experiments with anti-UVs windows.

5.5.4 Ozone

In all the simulations presented above, the O_3 concentrations are not altered by any change in NOx and HONO concentrations.

650   This is an expected behaviour, considering that the main source of O_3 is transport from outdoor, and that its main sink is deposition. Fig. 21 shows that variations in uptake coefficient γ_{O_3} modify the O_3 concentration significantly, and also the NO concentration by means of homogeneous chemistry. When γ_{O_3} tends to zero, the O_3 concentration increases up to a value very close to the experimental one, whereas the NO concentration decreases to concentrations much lower than those observed. With an uptake coefficient $\gamma_{\text{O}_3} = 10^{-6}$ and no desorption reaction for O_3, both O3 and NO are correctly modelled : albeit

655   lower than the experimental record, O_3 remains within 60% of the measured concentration, while the NO RMSE keeps close to one.

6   Modelling high NO_2 concentrations : focus on Experiment 1

When analyzing the optimized simulations, it can be noticed that the parameters fitting Experiments 2 and 3 are rather similar, but can significantly differ from some of those fitting Experiment 1, especially the ones controlling the adsorption/desorption

660   of the NOy compounds. The difficulty in simulating Experiment 1 (Fig. 6) lies in handling the fast transition from a moderate NO_2 concentration to a very high one. To prevent the HONO and NO secondary productions from rocketing after the NO_2

injection, $k'_{NO\,(ad)}$ was decreased and γ_{HONO} was increased so as to limit the NO and HONO releases. To preserve satisfying NO and HONO levels before the injection, the initial concentrations of $NO_{(ad)}$ and $HONO_{(ad)}$ were pushed up in order to counterbalance the weaker release of these species.

665   In spite of the above, changing the model parameters did not allow to completely mitigate the NO and HONO breakouts caused by the massive NO_2 supply. Previously, the modelling of the HONO production in high NO_2 conditions, *i.e.* NO_2 concentrations exceeding 25 ppb, was already pointed out by Mendez et al. (2017) as a challenging issue. Like in this study, the experimental HONO step up caused by the NO_2 injection was moderate, which existing model failed to replicate, by overestimating the HONO increase. Mendez et al. (2017) proposed to cope with that by introducing a compound SURF representing

670   the number of sites available for NO_2, thus limiting the amount of $NO_{2(ad)}$ for surface hydrolysis.

In this paper, a similar solution is implemented by extending the definition of SURF to all the surface compounds introduced in this model. Here SURF represents the number of sites available for NO, HONO, NO_2 and HNO_3. SURF is incorporated in the adsorption/desorption reactions, but only modifies the kinetics of these reactions when its "concentration" is less than unity. In other words, as long as lots of surface sites are available, the sorption dynamics behaves as usual, but as soon as the

675   surface approaches saturation, the kinetics of the adsorption reactions is increased of one order, in addition to be slowed down by the SURF "concentration" less than unity.

The resulting profiles are presented in Fig. 22, using the same parameters as the optimized simulation. The main differences with Mendez et al. (2017) are that the NO, NO_2 and O_3 concentrations are not fixed to their measured values, and that the first part of the HONO profile matches the experimental data. In this test, the NO_2 injection makes the three NOy compounds

680   uprise. The magnitude of this uprise is determined by the initial value of the SURF "concentration". When this value is very large, the concentration profiles converge to the optimized simulation (Fig. 6). It appears that limiting the sorption of NO_2 and related species generates an excess of gas-phase NOy which largely exceeds the decrease of NOy produced by heterogeneous chemistry. If the overestimation of the NO and HONO secondary formation cannot be mitigated by limiting the adsorption of gas-phase species, the most probable way to concile models and experiments may be to search for more complexe surface

685   processes that could account for that.

7   Discussion

Considering the number of parameters involved in this model, a given simulation result is likely reachable by several parameters combinations. Additionally, some parameters allowing to replicate the records presented in this study are typical of the room of the experiments and would be hardly transferable to other indoor environments. These are the filtration factor, the speed of

690   the air, the desorption constants and the uptake coefficients. Although these parameters are basically environment-dependent and non-unique, multiple conclusions can be drawn from these tests regarding the general principles of IAQ modelling.

The air mixing velocity introduced like in Mendez et al. (2017) appears as a critical parameter for the four main species leading the inorganic chemistry. The building filtration factor, generally taken as unity because barely studied, also stands as a determining factor. This parameter should not be confused with the ventilation rate (k_{AER}) which encompasses both the leaks

695 to outside and to the rest of the building. The building filtration factor is the fraction of air influx coming from outside the building. In these experiments, its value is far from unity, thus featuring airtight windows. Using a filtration factor of unity would have lead to overestimate the intake of outdoor pollutants, thus mitigating the importance of heterogenous phenomena.

The surface hydrolysis of NO_2 produces sorbed HONO and HNO_3 which further react to produce sorbed NO. The kinetics of this reaction is determined by its kinetic rate k_{S1}, and also by the NO_2 adsorption/desorption reactions which control the
700 variations of the $NO_{2(ad)}$ reservoir. The $NO_{2(ad)}$ concentration variations largely influence the variations of the other sorbed species concentrations through the means of reaction S_1, which can be considered as the cornerstone of indoor heterogeneous chemistry. Interestingly, a very small adjustment in the stoichiometry of reaction S_1 allows to increase the HONO secondary production significantly in all experiments.

The NO secondary production mainly derives from reaction S_2 which competes with the HONO desorption. The kinetic
705 rates of these reactions can be influenced by the nature of the surface materials. The release kinetics of these species flow from their sorbed concentrations, which likely depend on a variety of parameters. Such environment-dependence could explain why the yields in HONO and NO reported in the literature can vary a lot from one study to another (Finlayson-Pitts et al., 2003). Reactions S_3 and S_4 can influence the NOy concentration time variations, but their impacts seem less predominant.

Regarding the sorption dynamics, as almost entirely produced by heterogeneous chemistry, HONO is extremely sensitive
710 to the values of its uptake coefficient and desorption constant. Obviously, these parameters have antagonist effects which can neutralize each other. The proper calibration of these parameters can be oriented by the shape of the sorbed species profile, with respect to the gas-phase experimental one. Contrary to HONO, the NO concentration does not seem affected by the uptake coefficient γ_{NO}. Similarly to the radical HO, NO is likely too reactive to be affected by deposition. Therefore, like done in the literature, a very small deposition velocity appears well suited for NO, whatever its uptake coefficient.

715 The simulations presented in section 4 show that the desorption constants are the parameters which are the most difficult to set, especially for NO and HONO. The problem is less striking for NO_2 since the main source of NO_2 is transport from outdoor in these experiments. By using a common value of $k'_{HONO(ad)}$ for the three experiments (reference simulations), the simulated HONO concentrations show an overestimation of 95% and 78% for Experiments 1 and 3. Using the same $k'_{NO(ad)}$ in Experiments 2 and 3, the simulated NO concentrations remain as similar to the measured ones as using the optimized
720 parameters. However, it is impossible to use the same value in Experiment 1 without making the NO concentration increase well above the measured values.

Small variations in uptake coefficients and desorption constants can be supported by differences in wall cladding between experiments. In the first one, walls were naked, whereas in the subsequent ones, walls were covered by boards freshly coated with a paint made of the same organic matrix. According to Finlayson-Pitts et al. (2003), the composition of the surface film
725 of water can play an important role in determining the yields of NO and HONO, but the nature of the underlying material should not influence this chemistry, unless it is sufficiently reactive to modify the composition of the surface film. The surface topology can also influence the material adsorption capacity : experiments conducted by Wainman et al. (2001) to study the influence of the surface nature on the NO_2 hydrolysis showed that HONO concentrations were significantly enhanced when synthetic carpet was used instead of Teflon surfaces. They suggested this was caused by the greater surface quantity provided

730   by the carpet fibers, allowing more room for the reaction to occur. In this study, it could be argued that differences in roughness between the walls and the paint boards, combined with differences in uptake values, may account for variations of surface sorption capacity between the first and next experiments. However, these elements are not sufficient to support a difference in $k'_{NO\,(ad)}$ of almost three orders of magnitude (see Set 1 in Tab. 5).

In light of this, it can be inferred that using a more sophisticated parameterization of the desorption reactions may be a
735   possible way to improve this model. Namely, it could be necessary to take into account the multi-layer organization of the surface film, or the migration processes from the surface materials to the interface between the surface film and the gas phase. Such improvement may also be a solution to the problems observed after the NO_2 injection during Experiment 1. Like Mendez et al. (2017), we observe that the measured increase of HONO after the NO_2 injection is moderate, and like the models tested by Mendez et al. (2017), the H^2I model overestimates this increase of HONO concentration. Implementing a deposition saturation
740   effect did not allow to improve the model's performance, but it can be hypothesized that a release limitation owing to the surface film structure may do so.

Finally, apart from the particular case of the HONO secondary production in high NO_2 conditions, the H^2I model successfully replicates the chemistry of inorganic species. We recall that, the VOCs concentrations were compelled to follow the experimental records. The simulations presented in section 4 show that a correct inorganic modelling associated to fixed VOCs
745   concentration yield a correct prediction of the HOx variations. In addition, the HOx profiles corresponding to the simulations presented in the sensitivity study are provided in Appendix A. Several observations can be made. First, all of the tests showing a combined increase of NO and NO_2 (Figs. 10-15 and Fig. 18) result in an increase of HO combined with a decrease of HO_2, whatever the HONO variations. Then, when O_3 is increased (Fig. 21), NO decreases without significant change in NO_2, while HO_2 experiences a substantial rise. The strong influence of O_3 on HO_2 is confirmed by Fig. 9 and Fig. 16; despite showing
750   the same NOx variations, their HO_2 variations are opposite, likely because of O_3 which increases in Fig. 9, thus pushing up HO_2. These behaviors are in agreement with the well-known gas-phase chemistry. At last, when none of the NOx is varied (Figs. 19-20), no HOx variation is observed, albeit significant HONO fluctuations. In these experiments, the presence of anti-UVs windows neutralizes the light wavelengths for which the HONO photolysis can produce radicals.

8   Conclusions

755   In this paper, a new numerical model combining homogeneous and heterogeneous chemistry is implemented and proved able to replicate the concentrations of inorganic compounds. For the first time, O_3, HONO, NOx and HOx species are simulated all at once and compared to experimental records acquired in a real room. The specificity of this model is to incorporate secondary reactions which were highlighted by laboratory studies but which are still absent from numerical models. It is also the first two-box model allowing to consider the variations of direct and indirect light throughout the day. The comparison between
760   the simulation results and experimental data allowed to tune the model parameters, which lead to several conclusions : (i) the building filtration factor and the speed of air mixing are important parameters which should deserve more attention; (ii) for the simulation duration considered (a third of day in average), the proper assessment of initial concentrations is critical; (iii)

whereas deposition and surface reactivity are treated together by current models, the distinction between sorption and surface reactions appears as essential. This distinction is based on the introduction of sorbed species which also have the possibility to desorb. To better constrain these sorption/desorption processes, there is a need of surface material characterization, especially measurements of O_3, NO_2 and HONO uptake coefficients and NO, NO_2 and HONO desorption constants, in various conditions of temperature, humidity and irradiation; (iv) the success of this model in simulating inorganic species largely arises from the better consideration of surface chemistry, thus highlighting its critical importance for indoor air reactivity. Whereas reactions S_3 and S_4 could be considered of secondary importance, reaction S_2 appears as important as reaction S_1 which is currently the only surface reaction taken into account by IAQ models. Reaction S_2 may account for unexplained variations in NO vs. HONO production ratios and should clearly be integrated. In the future, the further understanding of heterogenous phenomena will be a necessary step toward the improvement of IAQ models.

Code availability. Code available at https://gitlab.enpc.fr/cerea/h2i

Author contributions. HW and KS conceived the project. EAF, KS and HW developed the methodology. EAF and KS developed the code. EAF made formal analysis and visualization. EAF, KS and HW performed investigations. EAF wrote the original draft. KS and HW reviewed the draft. HW acquired the funding.

Competing interests. The authors declare that they have no conflict of interest.

Acknowledgements. This work was supported by the LABEX SERENADE (no. ANR-11-LABX-0064) funded by the "Investissements d'Avenir" program of the French National Research Agency.

780 **References**

Ambrose, D. and Ghiassee, N.: Vapour pressures and critical temperatures and critical pressures of some alkanoic acids: C1 to C10, The Journal of Chemical Thermodynamics, 19, 505–519, 1987.

Ambrose, D., Broderick, B. E., and Townsend, R.: The critical temperatures and pressures of thirty organic compounds, Journal of Applied Chemistry and Biotechnology, 24, 359–372, 1974a.

785 Ambrose, D., Sprake, C., and Townsend, R.: Thermodynamic properties of organic oxygen compounds XXXIII. The vapour pressure of acetone, The Journal of Chemical Thermodynamics, 6, 693–700, 1974b.

Ambrose, D., Connett, J., Green, J., Hales, J., Head, A., and Martin, J.: Thermodynamic properties of organic oxygen compounds 42. Physical and thermodynamic properties of benzaldehyde, The Journal of Chemical Thermodynamics, 7, 1143–1157, 1975.

Ascher, U. and Petzold, L.: Computer Methods for Ordinary Differential Equations and Differential-Algebraic Equations, ISBN 978-0-
790 89871-412-8., Philadelphia: Society for Industrial and Applied Mathematics, 1998.

Carslaw, N.: A new detailed chemical model for indoor air pollution, Atmospheric Environment, 41, 1164–1179, 2007.

Carter, W.: Development of the SAPRC-07 chemical mechanism, Atmos. Environ., 44, 5324–5335, 2010.

Chen, N. H. and Othmer, D. F.: New generalized equation for gas diffusion coefficient., Journal of Chemical and Engineering Data, 7, 37–41, 1962.

795 Courtey, S., Blondeau, P., Jouandon, E., and Allard, F.: Modeling of the production of secondary gaseous products in confined atmospheres, Building and Environment, 44, 1343–1349, 2009.

Delaunois, C.: Effect of the Filling Rate of a Reactor on the Vapor Tension and the Temperature at the Beginning of Cracking of Phenols at High Pressures, Ann. Mines Belg., pp. 9–16, 1968.

D'Souza, R. and Teja, A.: The prediction of the vapor pressures of carboxylic acids, Chemical engineering communications, 61, 13–22,
800 1987.

Falls, A. and Seinfeld, J.: Continued development of a kinetic mechanism for photochemical smog, Environmental Science & Technology, 12, 1398–1406, 1978.

Febo, A. and Perrino, C.: Prediction and experimental evidence for high air concentration of nitrous acid in indoor environments, Atmospheric Environment. Part A. General Topics, 25, 1055–1061, 1991.

805 Finlayson-Pitts, B., Wingen, L., Sumner, A., Syomin, D., and Ramazan, K.: The heterogeneous hydrolysis of NO 2 in laboratory systems and in outdoor and indoor atmospheres: An integrated mechanism, Physical Chemistry Chemical Physics, 5, 223–242, 2003.

Furtaw Jr., E. J., Pandian, M. D., Nelson, D. R., and Behar, J. V.: Modeling indoor air concentrations near emission sources in imperfectly mixed rooms, Journal of the Air & Waste Management Association, 46, 861–868, 1996.

Gandolfo, A.: Incidence de la chimie hétérogène des oxydes d'azote sur la qualité des atmosphères intérieures: impacts des nanoparticules
810 de TiO2 dans les peintures, Ph.D. thesis, Aix-Marseille University, 2018.

Gandolfo, A., Bartolomei, V., Alvarez, E. G., Tlili, S., Gligorovski, S., Kleffmann, J., and Wortham, H.: The effectiveness of indoor photocatalytic paints on NOx and HONO levels, Applied Catalysis B: Environmental, 166, 84–90, 2015.

Gandolfo, A., Gligorovski, V., Bartolomei, V., Tlili, S., Alvarez, E. G., Wortham, H., Kleffmann, J., and Gligorovski, S.: Spectrally resolved actinic flux and photolysis frequencies of key species within an indoor environment, Building and Environment, 109, 50–57, 2016.

815 Gandolfo, A., Rouyer, L., Wortham, H., and Gligorovski, S.: The influence of wall temperature on NO2 removal and HONO levels released by indoor photocatalytic paints, Applied Catalysis B: Environmental, 209, 429–436, 2017.

Gery, M., Whitten, G., Killus, J., and Dodge, M.: A photochemical kinetics mechanism for urban and regional scale computer modeling, J. Geophys. Res.-Atmos., 94, 12 925–12 956, 1989.

Glaser, F. and Rüland, H.: Untersuchungen über Dampfdruckkurven und kritische Daten einiger technisch wichtiger organischer Substanzen, Chemie Ingenieur Technik, 29, 772–775, 1957.

Goliff, W. S., Stockwell, W. R., and Lawson, C. V.: The regional atmospheric chemistry mechanism, version 2, Atmospheric environment, 68, 174–185, 2013.

Grøntoft, T. and Raychaudhuri, M. R.: Compilation of tables of surface deposition velocities for O3, NO2 and SO2 to a range of indoor surfaces, Atmospheric Environment, 38, 533–544, 2004.

Gude, M. and Teja, A.: The critical properties of several n-alkanols, tetralin and NMP, Experimental Results for DIPPR 1990-1991 Projects on Phase Equilibria and Pure Components Properties, pp. 174–183, 1994.

Gude, M. and Teja, A. S.: Vapor-liquid critical properties of elements and compounds. 4. Aliphatic alkanols, Journal of Chemical and Engineering Data, 40, 1025–1036, 1995.

Holland, F., Hofzumahaus, A., Schäfer, J., Kraus, A., and Pätz, H.-W.: Measurements of OH and HO2 radical concentrations and photolysis frequencies during BERLIOZ, J. Geophys. Res.-Atmos., 108, PHO–2, 2003.

Jenkins, A. C. and Birdsall, C. M.: The vapor pressures and critical constants of pure ozone, The Journal of Chemical Physics, 20, 1158–1161, 1952.

Joback, K. G. and Reid, R. C.: Estimation of pure-component properties from group-contributions, Chemical Engineering Communications, 57, 233–243, 1987.

Kaper, H. and Ferziger, J. H.: Mathematical theory of transport processes in gases, North-Holland Publishing, 1972.

Kim, Y., Sartelet, K., and Seigneur, C.: Comparison of two gas-phase chemical kinetic mechanisms of ozone formation over Europe, Journal of atmospheric chemistry, 62, 89–119, 2009.

Kukui, A., Ancellet, G., and Le Bras, G.: Chemical ionisation mass spectrometer for measurements of OH and Peroxy radical concentrations in moderately polluted atmospheres, Journal of atmospheric chemistry, 61, 133–154, 2008.

Lai, A. C. and Nazaroff, W. W.: Modeling indoor particle deposition from turbulent flow onto smooth surfaces, Journal of aerosol science, 31, 463–476, 2000.

LCE: Qualification and distribution of the actinic photon flux within indoor environment: advance for indoor air chemistry modeling, in prep.

Lide, D. R.: CRC handbook of chemistry and physics, Internet Version 2005, <http://www.hbcpnetbase.com>, CRC Press, Boca Raton, FL, 2005.

Linstrom, P. and Mallard, W.: NIST Chemistry WebBook, NIST Standard Reference Database Number 69, National Institute of Standards and Technology, Gaithersburg MD, 20899, https://doi.org/10.18434/T4D303.

McQuiston, F. C., Parker, J. D., and Spitler, J. D.: Heating, ventilating, and air conditioning: analysis and design, John Wiley & Sons, 2004.

Mendez, M., Blond, N., Blondeau, P., Schoemaecker, C., and Hauglustaine, D. A.: Assessment of the impact of oxidation processes on indoor air pollution using the new time-resolved INCA-Indoor model, Atmospheric Environment, 122, 521–530, 2015.

Mendez, M., Blond, N., Amedro, D., Hauglustaine, D. A., Blondeau, P., Afif, C., Fittschen, C., and Schoemaecker, C.: Assessment of indoor HONO formation mechanisms based on in situ measurements and modeling, Indoor air, 27, 443–451, 2017.

Mochida, M. and Finlayson-Pitts, B. J.: FTIR Studies of the Reaction of Gaseous NO with HNO3 on Porous Glass: Implications for Conversion of HNO3 to Photochemically Active NO x in the Atmosphere, The Journal of Physical Chemistry A, 104, 9705–9711, 2000.

Nazaroff, W. W. and Cass, G. R.: Mathematical modeling of chemically reactive pollutants in indoor air, Environmental Science & Technology, 20, 924–934, 1986.

Nikitin, E. D., Pavlov, P. A., Popov, A. P., and Nikitina, H. E.: Critical properties of hydrogen peroxide determined from direct measurements, The Journal of Chemical Thermodynamics, 27, 945–952, 1995.

Ramazan, K. A., Syomin, D., and Finlayson-Pitts, B. J.: The photochemical production of HONO during the heterogeneous hydrolysis of NO 2, Physical Chemistry Chemical Physics, 6, 3836–3843, 2004.

Ravindran, P., Davis, E., and Ray, A.: Diffusivities of low-volatility species in light gases, AIChE Journal, 25, 966–975, 1979.

Rosenbrock, H.: Some general implicit processes for the numerical solution of differential equations, The Computer Journal, 5, 329–330, 1963.

Sandu, A., Verwer, J., Blom, J., Spee, E., Carmichael, G., and Potra, F.: Benchmarking stiff ode solvers for atmospheric chemistry problems II: Rosenbrock solvers, Atmos. Environ., 31, 3459–3472, 1997.

Sartelet, K., Hayami, H., Albriet, B., and Sportisse, B.: Development and preliminary validation of a modal aerosol model for tropospheric chemistry: MAM, Aerosol Sci. Tech., 40, 118–127, 2006.

Sarwar, G., Corsi, R., Kimura, Y., Allen, D., and Weschler, C. J.: Hydroxyl radicals in indoor environments, Atmospheric Environment, 36, 3973–3988, 2002.

Sato, H., Watanabe, K., Levelt Sengers, J., Gallagher, J., Hill, P., Straub, J., and Wagner, W.: Sixteen thousand evaluated experimental thermodynamic property data for water and steam, Journal of physical and chemical reference data, 20, 1023–1044, 1991.

Shen, H., Tan, H., and Tzempelikos, A.: The effect of reflective coatings on building surface temperatures, indoor environment and energy consumption—An experimental study, Energy and Buildings, 43, 573–580, 2011.

Stockwell, W., Middleton, P., Chang, J., and Tang, X.: The 2nd generation regional acid deposition model chemical mechanism for regional air quality modeling, J. Geophys. Res.-Atmos., 95, 16 343–16 367, 1990.

Teja, A. and Anselme, M.: The critical properties of thermally stable and unstable fluids. I. 1985 results, in: AIChE Symp. Ser, vol. 86, pp. 115–121, 1990.

Tsonopoulos, C. and Ambrose, D.: Vapor-liquid critical properties of elements and compounds. 3. Aromatic hydrocarbons, Journal of Chemical and Engineering Data, 40, 547–558, 1995.

Wainman, T., Weschler, C. J., Lioy, P. J., and Zhang, J.: Effects of surface type and relative humidity on the production and concentration of nitrous acid in a model indoor environment, Environmental science & technology, 35, 2200–2206, 2001.

Weschler, C.: Chemistry in indoor environments: 20 years of research, Indoor Air, 21, 205–218, 2011.

Weschler, C. J. and Shields, H. C.: Production of the hydroxyl radical in indoor air, Environmental Science & Technology, 30, 3250–3258, 1996.

Weschler, C. J., Shields, H. C., and Naik, D. V.: Indoor chemistry involving O3, NO, and NO2 as evidenced by 14 months of measurements at a site in Southern California, Environmental Science & Technology, 28, 2120–2132, 1994.

Yarwood, G., Rao, S., Yocke, M., and Whitten, G.: Updates to the Carbon Bond Chemical Mechanism: CB05 Final Report to the US EPA, RT-0400675, available at http://www.camx.com/publ/pdfs/CB05_Final_Report_120805.pdf, 2005.

Table 1. Heterogeneous reactions added to the RACM2 model. The symbol χ designates the species that undergoes unimolecular decomposition. These species are the VOCs (see Tab. 2 for the list of considered VOCs), O_3, NO_3, HNO_4 and H_2O_2. Reactions S_1, S_2, S_3 and S_4 are the model equivalent of reactions R1, R3, R2 and R4.

Reactions	Kinetic constants
Unimolecular decomposition	
$\chi \rightarrow$	k_χ
Adsorption reactions	
$NO \rightarrow NO_{(ad)}$	k_{NO}
$NO_2 \rightarrow NO_{2\,(ad)}$	k_{NO_2}
$HONO \rightarrow HONO_{(ad)}$	k_{HONO}
$HNO_3 \rightarrow HNO_{3\,(ad)}$	k_{HNO_3}
Desorption reactions	
$NO_{(ad)} \rightarrow NO$	$k_{NO\,(ad)}$
$NO_{2\,(ad)} \rightarrow NO_2$	$k_{NO_2\,(ad)}$
$HONO_{(ad)} \rightarrow HONO$	$k_{HONO\,(ad)}$
Surface reactions	
$NO_{2\,(ad)} \rightarrow 0.5\ HNO_{3(ad)} + 0.5\ HONO_{(ad)}$	k_{S1}
$HONO_{(ad)} + HNO_{3(ad)} \rightarrow 2\ NO_{(ad)}$	k_{S2}
$HONO_{(ad)} \rightarrow 0.5\ NO_{(ad)} + 0.5\ NO_{2\,(ad)}$	k_{S3}
$NO_{(ad)} + HNO_{3(ad)} \rightarrow NO_{2\,(ad)} + HONO_{(ad)}$	k_{S4}

Table 2. RACM2 molar mass M [g.mol^{-1}], critical temperature T_c [K] and critical molar volume V_c [cm^3.mol^{-1}] of a species representing the RACM2 compound and diffusion coefficient D [m^2.s^{-1}] computed following the procedure described in section 2.4.1. The references listed are available from the NIST webbook (Linstrom and Mallard).

Compounds	M	Representative species	T_c	V_c	Reference	D (10^{-5})
OLT	42	Propene	364.90	185	Lide (2005)	1.18
OLI	68	Pentene	464.80	298	Lide (2005)	0.833
TOL	92	Toluene	822.28	490	-	0.573
XYL	106	m-Xylene	617.00	375	Tsonopoulos and Ambrose (1995)	0.674
HCHO	30	Formaldehyde	436.48	100	-	1.61
ALD	58	Propanal	504.40	204	Gude and Teja (1994)	1.01
KET	86	2-Pentanone	561.08	320	Ambrose et al. (1974a)	0.758
ISO	68	Isoprene	480.20	280	-	0.855
CSL	108	Cresol	695.15	290	Glaser and Rüland (1957)	0.752
ORA1	46	Formic acid	588.00	130	Ambrose and Ghiassee (1987)	1.26
ORA2	60	Acetic acid	590.70	171	D'Souza and Teja (1987)	1.07
MACR	70	Methacrolein	516.54	260	-	0.874
MOH	32	Methanol	512.50	117	Gude and Teja (1994)	1.45
ACD	44	Acetaldehyde	466.00	154	Teja and Anselme (1990)	1.22
ACT	58	Acetone	508.10	213	Ambrose et al. (1974b)	0.991
BEN	78	Benzene	562.05	256	Tsonopoulos and Ambrose (1995)	0.857
PHEN	94	Phenol	694.30	230	Delaunois (1968)	0.855
BALD	106	Benzaldehyde	695.00	340	Ambrose et al. (1975)	0.697
ROH	60	Butanol	563.00	274	Gude and Teja (1995)	0.862
UALD	84	Pentenal	548.86	310	-	0.775
LIM	136	Limonene	657.16	500	-	0.562
O$_3$	48	O$_3$	261.10	89	Jenkins and Birdsall (1952)	1.64
NO	30	NO	180.00	58	Lide (2005)	2.25
NO$_2$	46	NO$_2$	561.53	110	-	1.36
HONO	47	NO$_2$	561.53	110	-	1.36
NO$_3$	62	NO$_3$	534.15	140	-	1.18
HNO$_3$	63	HNO$_3$	648.46	140	-	1.14
HNO$_4$	79	HNO$_4$	669.82	155	-	1.05
HO	17	H$_2$O	647.10	56	Sato et al. (1991)	2.24
HO$_2$	33	H$_2$O$_2$	728.00	70	Nikitin et al. (1995)	1.69
H$_2$O$_2$	34	H$_2$O$_2$	728.00	70	Nikitin et al. (1995)	1.68

Table 3. Parameters of the experiments : total duration, k_{AER}, minimum and maximum temperature and humidity, type of paint.

Experiments	Day	Duration [h]	k_{AER}	T_{min} [°C]	T_{max} [°C]	H_{min} [%]	H_{max} [%]	Type of paint
Experiment 1	27 October	8.7	0.25	22.7	26.7	42	44	No paint board
Experiment 2	28 October	6.2	0.29	24.3	27.8	39	45	0% TiO_2
Experiment 3	29 October	7.9	0.19	21.4	27.1	44	49	3.5% TiO_2

Table 4. List of the RACM2 compounds initialized. Definition, carbon valence and concentrations at the start of the experiments in μg.m^{-3}. Compounds marked with a symbol (*) were not measured experimentally, but were estimated based on simulations, so as to assess their importance regarding initial conditions (see section 3.1).

Species	Definition	Carbon #	Exp1	Exp2	Exp3
	Organic compounds				
ACD	Acetaldehyde	2	15.78	30.16	39.95
ACT	Acetone	3	11.77	18.80	18.30
ALD	C3 and higher aldehydes	3	22.18	63.31	107.0
BALD	Benzaldehyde and other aromatic aldehydes	7	0.559	2.437	5.879
BEN	Benzene	6	1.220	2.127	2.203
CO	Carbon monoxide (*)	1	0.535	0.517	3.581
CSL	Cresol and other hydroxy substituted aromatics	7	0.010	0.129	0.239
DCB1	Unsaturated dicarbonyls (*)	4.5	0.238	0.336	0.888
DCB2	Unsaturated dicarbonyls (*)	7	0.375	0.530	1.403
DCB3	Unsaturated dicarbonyls (*)	4	0.452	0.643	1.849
HCHO	Formaldehyde	1	34.88	42.88	51.58
ISO	Isoprene	5	0.314	0.747	1.160
KET	Ketones	5	3.002	8.503	11.50
LIM	d-limonene and other cyclic diene-terpenes	10	6.151	8.799	8.273
MACR	Methacrolein	4	3.289	4.803	5.093
MGLY	Peroxy radicals formed from MEK (*)	3	0.355	0.415	1.640
MOH	Methanol	1	15.29	25.90	38.72
OLI	Internal alkenes	5	2.910	7.802	15.55
OLT	Terminal alkenes	3.8	20.20	35.33	62.52
ORA1	Formic acid	1	30.52	33.10	30.74
ORA2	Acetic acid and higher acids	2	74.17	123.1	168.1
PAN	Peroxyacetyl nitrate and higher saturated PANs (*)	2	0.360	0.107	1.511
PHEN	Phenol	6	0.554	0.567	0.585
PPN	Peroxypropionyl nitrate (*)	3	0.483	0.195	3.978
ROH	C3 and higher alcohols	3	10.32	43.99	105.0
UALD	Unsaturated aldehydes	5	0.687	1.385	1.968
TOL	Toluene and less reactive aromatics	7.1	3.580	4.702	4.684
XYL	Xylene and less reactive aromatics	8.9	31.37	62.72	38.48
	Inorganic compounds				
HONO	Nitrous acid		2.706	4.560	2.384
NO	Nitric oxide		1.344	5.352	3.226
NO2	Nitrogen dioxide		12.02	5.087	9.184
O3	Ozone		2.767	0.000	0.992
	Radicals				
HO	Hydroxy radical		4.73×10^{-6}	7.72×10^{-6}	1.64×10^{-5}
HO2	Hydroperoxy radical		7.84×10^{-4}	5.00×10^{-4}	2.58×10^{-3}

Table 5. Parameter values for each type of simulation and each experiment. The parameters are : filtration factor [-], speed of air [m.s^{-1}], NO_2 hydrolysis stoichiometric coefficients [-], uptake coefficients γ_i [-], surface reactions kinetic rates k_S [s^{-1}], desorption reactions kinetic rates $k'_{i,(ad)}$ [s^{-1} .mlc^{-1}]. Set 1 refers to the simulations with optimized parameters, Set 2 refers to the simulations with common k_S constants, Set 3 refers to the simulations with common parameter values. The factor f is allowed to vary between experiments; for the rest of the parameters, all of the values that differ from the Set 3 solution are denoted in bold.

Set of parameters	Set 1			Set 2			Set 3		
Experiment	Exp 1	Exp 2	Exp3	Exp 1	Exp 2	Exp3	Exp 1	Exp 2	Exp3
f	0.25	0.33	0.30	0.25	0.33	0.30	0.25	0.33	0.30
u_{inf}	0.24	0.24	0.24	0.24	0.24	0.24	0.24	0.24	0.24
β_{HNO_3}	0.47	0.47	0.47	0.47	0.47	0.47	0.47	0.47	0.47
β_{HONO}	0.53	0.53	0.53	0.53	0.53	0.53	0.53	0.53	0.53
γ_{NO}	8×10^{-9}	8×10^{-9}	8×10^{-9}	8×10^{-9}	8×10^{-9}	8×10^{-9}	8×10^{-9}	8×10^{-9}	8×10^{-9}
γ_{NO_2}	$\mathbf{1.5 \times 10^{-6}}$	5×10^{-6}	5×10^{-6}	5×10^{-6}	5×10^{-6}	5×10^{-6}	5×10^{-6}	5×10^{-6}	5×10^{-6}
γ_{HONO}	$\mathbf{7 \times 10^{-7}}$	2×10^{-8}	2×10^{-8}	2×10^{-8}	2×10^{-8}	2×10^{-8}	2×10^{-8}	2×10^{-8}	2×10^{-8}
γ_{O_3}	1×10^{-6}	1×10^{-6}	1×10^{-6}	1×10^{-6}	1×10^{-6}	1×10^{-6}	1×10^{-6}	1×10^{-6}	1×10^{-6}
k_{S1}	$\mathbf{5 \times 10^{-4}}$	3×10^{-3}	3×10^{-3}	3×10^{-3}	3×10^{-3}	3×10^{-3}	3×10^{-3}	3×10^{-3}	3×10^{-3}
k_{S2}	$\mathbf{1 \times 10^{-14}}$	$\mathbf{4 \times 10^{-14}}$	$\mathbf{4 \times 10^{-13}}$	1×10^{-13}	1×10^{-13}	1×10^{-13}	1×10^{-13}	1×10^{-13}	1×10^{-13}
k_{S3}	$\mathbf{5 \times 10^{-5}}$	1×10^{-5}	1×10^{-5}	1×10^{-5}	1×10^{-5}	1×10^{-5}	1×10^{-5}	1×10^{-5}	1×10^{-5}
k_{S4}	2×10^{-15}	2×10^{-15}	2×10^{-15}	2×10^{-15}	2×10^{-15}	2×10^{-15}	2×10^{-15}	2×10^{-15}	2×10^{-15}
$k'_{NO(ad)}$	$\mathbf{7 \times 10^{-23}}$	$\mathbf{6 \times 10^{-21}}$	$\mathbf{3 \times 10^{-20}}$	$\mathbf{2 \times 10^{-22}}$	$\mathbf{3 \times 10^{-21}}$	8×10^{-21}	$\mathbf{2 \times 10^{-22}}$	8×10^{-21}	8×10^{-21}
$k'_{NO_2(ad)}$	$\mathbf{1 \times 10^{-23}}$	1×10^{-22}	1×10^{-22}	1×10^{-22}	1×10^{-22}	1×10^{-22}	1×10^{-22}	1×10^{-22}	1×10^{-22}
$k'_{HONO(ad)}$	$\mathbf{2.5 \times 10^{-22}}$	$\mathbf{4.5 \times 10^{-22}}$	$\mathbf{1.5 \times 10^{-22}}$	$\mathbf{3 \times 10^{-22}}$	$\mathbf{7 \times 10^{-22}}$	$\mathbf{1.2 \times 10^{-22}}$	5×10^{-22}	5×10^{-22}	5×10^{-22}

Table 6. Simulations evaluations with respect to the four modelled inorganic compounds : simulated average, relative error between simulated and measured average, Root-Mean-Square Error (RMSE), Mean Normalized Gross Error (MNGE) and Mean Normalized Bias Error (MNBE).

Experiment	Exp 1					Exp 2					Exp 3				
Species	O_3	NO	NO_2	HONO	NOx	O_3	NO	NO_2	HONO	NOx	O_3	NO	NO_2	HONO	NOx
Measured average [$\mu g.m^{-3}$]	1.51	1.42	5.48	3.64	9.13	1.52	4.81	4.24	5.56	9.06	1.81	2.93	4.83	3.70	7.77
Set 1															
Simulated average [$\mu g.m^{-3}$]	0.76	0.82	2.68	3.55	3.50	0.65	4.36	4.57	5.52	8.94	0.73	2.07	5.88	3.64	7.96
Relative error [%]	49.66	42.25	51.09	2.47	61.66	57.23	9.35	7.78	0.71	1.32	59.66	29.35	21.73	1.62	2.44
RMSE [$\mu g.m^{-3}$]	0.99	0.68	3.43	0.12	5.80	1.80	0.98	0.95	0.15	0.45	1.45	0.98	1.26	0.16	0.47
MNGE [%]	47.21	43.65	45.15	2.60	62.34	56.68	16.03	21.33	1.09	4.12	57.97	33.35	28.91	3.42	5.32
MNBE [%]	-45.83	-43.35	-45.15	-2.41	-62.34	-26.99	-9.07	11.40	-0.07	-1.33	-52.79	-31.52	26.59	-0.38	2.55
Set 2															
Simulated average [$\mu g.m^{-3}$]	0.68	1.13	2.17	3.64	3.31	0.67	4.16	4.50	5.50	8.66	0.73	2.01	5.84	3.58	7.86
Relative error [%]	54.96	20.42	60.4	0.00	63.74	55.92	13.51	6.13	1.07	4.41	59.66	31.39	20.91	3.24	1.15
RMSE [$\mu g.m^{-3}$]	1.05	0.51	4.03	0.15	6.01	1.78	1.11	0.89	0.20	0.60	1.45	1.01	1.25	0.16	0.58
MNGE [%]	52.33	33.3	53.07	3.34	63.94	56.02	18.00	20.11	2.47	5.93	57.77	33.66	28.76	3.14	6.25
MNBE [%]	-51.45	-22.77	-53.07	-0.09	-63.94	-24.82	-13.53	9.54	-0.67	-4.48	-52.59	-32.82	26.08	-1.92	1.74
Set 3															
Simulated average [$\mu g.m^{-3}$]	0.68	1.14	2.12	7.16	3.26	0.61	4.74	4.70	5.04	9.45	0.75	1.93	5.63	6.56	7.56
Relative error [%]	54.96	19.71	61.31	96.7	64.29	59.86	1.45	10.84	9.35	4.30	58.56	34.12	16.56	77.29	2.70
RMSE [$\mu g.m^{-3}$]	1.05	0.52	4.06	3.76	6.04	1.83	0.88	1.05	0.57	0.69	1.43	1.11	1.02	3.09	0.46
MNGE [%]	52.48	34.28	54.61	94.21	64.63	58.70	16.96	23.44	8.24	6.39	57.18	38.45	22.54	78.34	5.15
MNBE [%]	-51.61	-22.99	-54.61	94.21	-64.63	-30.44	-0.20	14.48	-8.23	4.41	-51.48	-36.82	20.15	78.29	-3.27
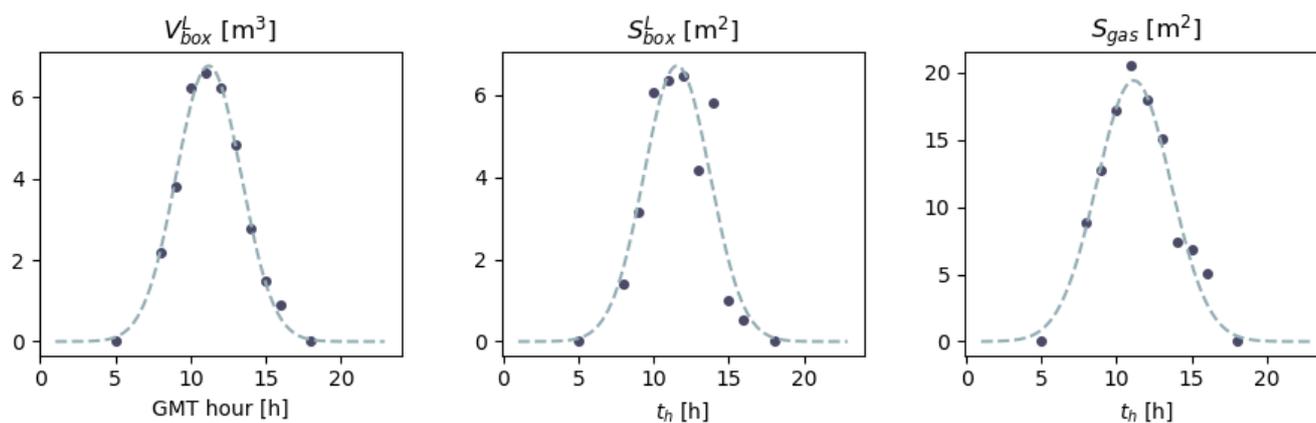
Figure 1. From the left to the right : evolution of V_{box}^L, S_{box}^L and S_{gas} with GMT hour. The solid circles denote the values estimated numerically, the dashed lines are the gaussian laws they allow to infer. These parameterizations are representative of the time period (27th to 31th October) and location (Martigues, France) of the experiments.
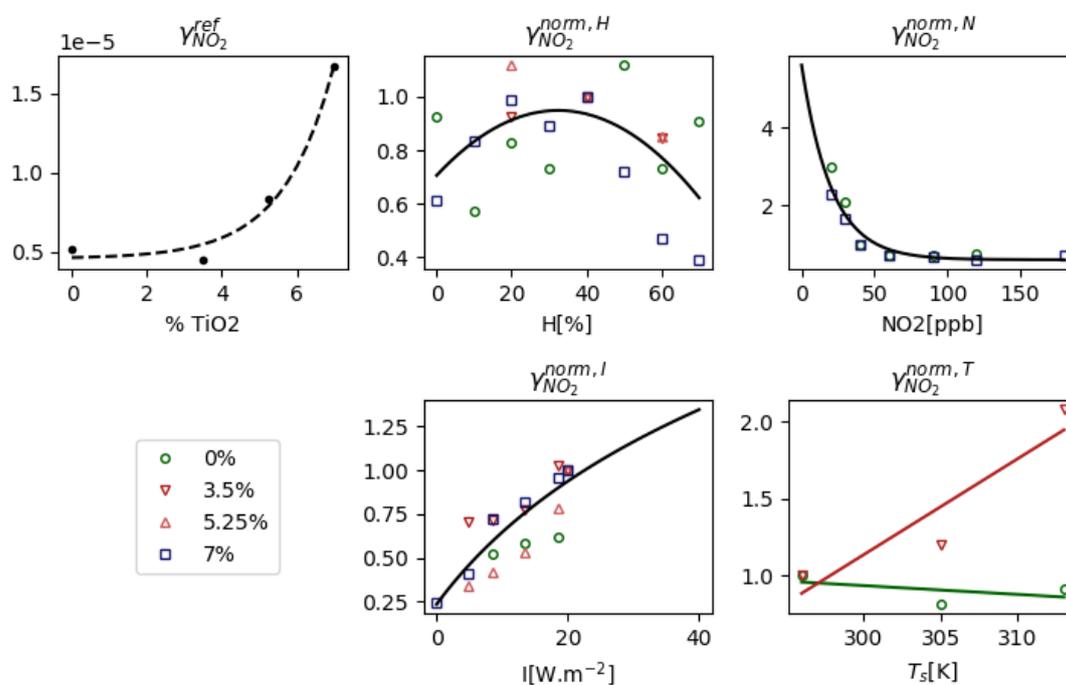
Figure 2. Evolution of γ_{NO_2}. The dots denote measurements, the open symbols denote normalized measurements (see text for details). The solid lines denote the parameterization as a function of H, N, I and T_s (Eqs. 25-28).
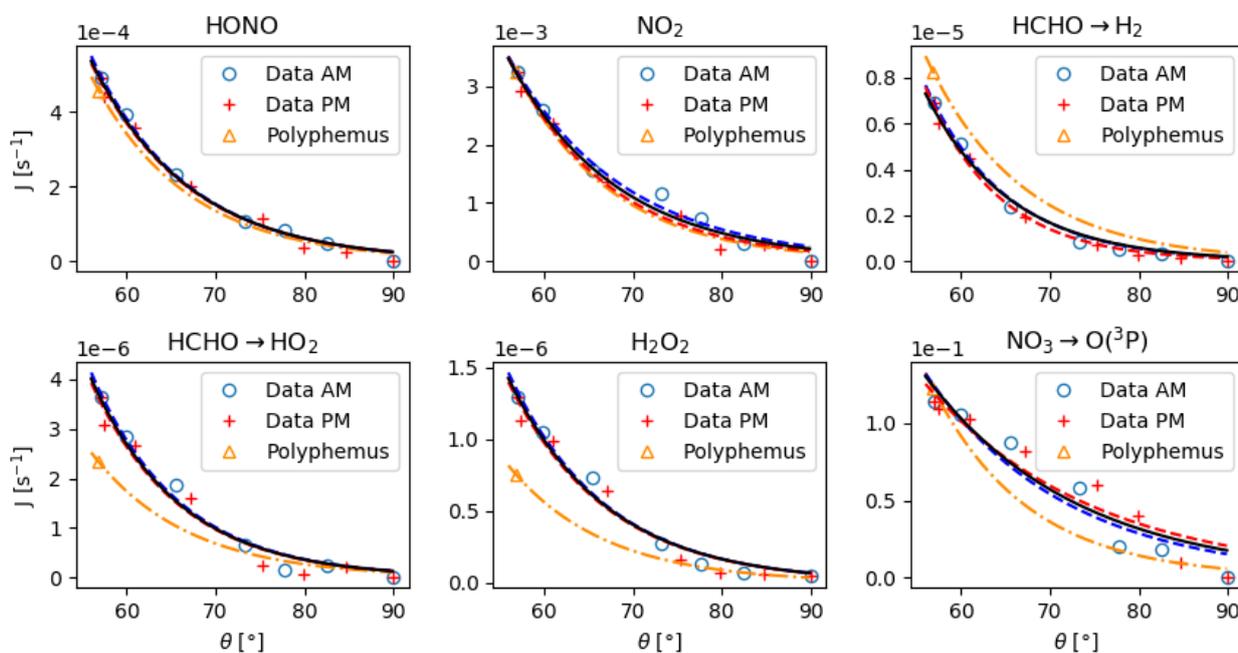
Figure 3. Photolysis rates as a function of zenith angle. The symbols '∘' and '+' denote the experimental rates acquired on the 30th October, in the morning and in the afternoon. The blue and red dashed lines are their parameterization using Eq. (31). The black solid line is the curve obtained by fitting both the data of the morning and those of the afternoon. The symbols '△' are the photolysis rates calculated with Eq. (30) with the cross sections and quantum yields taken from Polyphemus. The yellow dash-dotted line is the deriving evolution of J with θ according to Eq. (33).
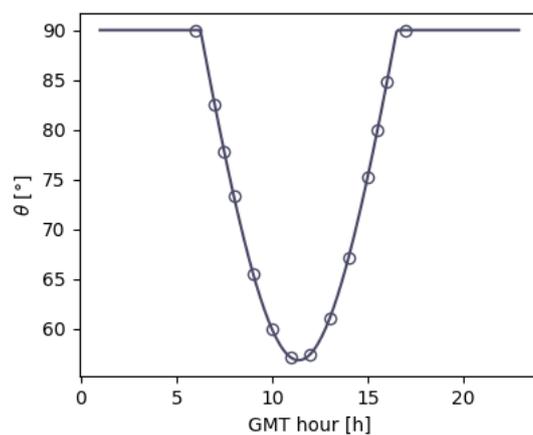
Figure 4. Zenith angle θ as a function of day hour, on the 27th October at latitude $43.41°$ and longitude $5.06°$ (Martigues area). The '$\circ$' symbols denote the hours of the J_i measurements by the spectroradiometer.
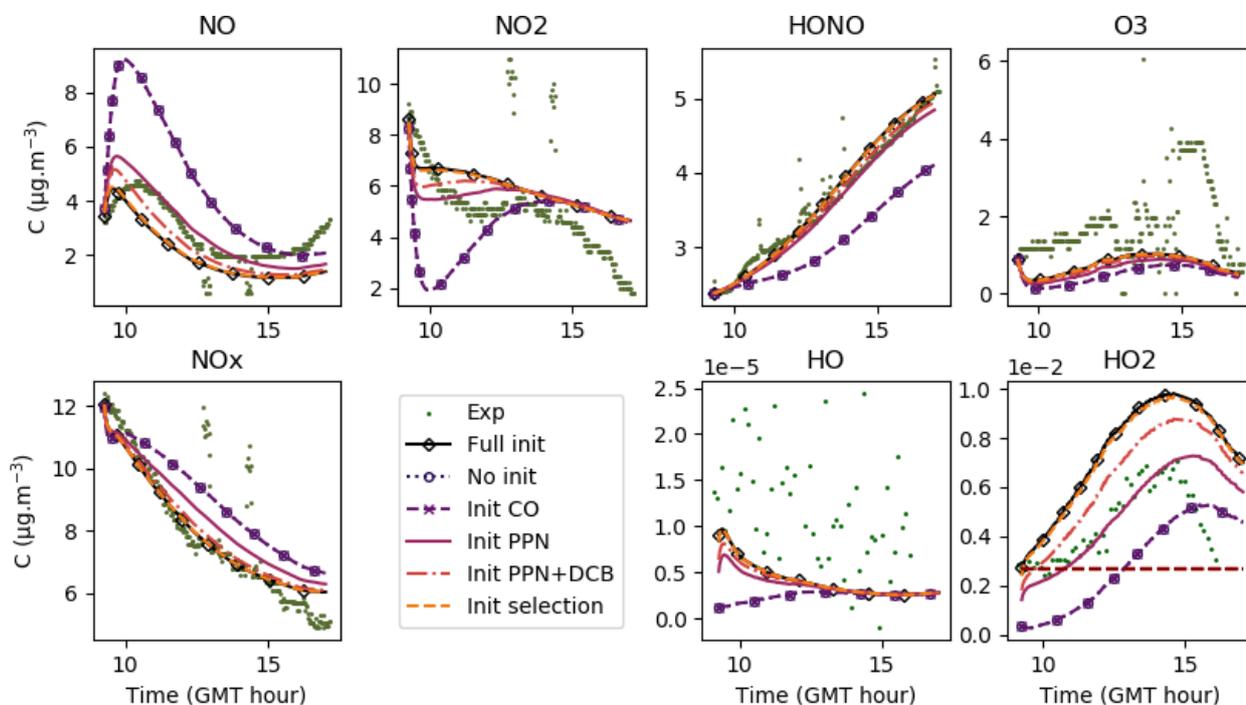
Figure 5. Inorganic and radical profiles for different initial conditions. The dots denote the experimental measurements (Experiment 3). In the bottom-right plot, the horizontal dashed line denotes the HO_2 concentration at the start of the measurements. "No init" means that all the compounds which were not detected during the campaign are a given a zero concentration at the start of the simulation. "Full init" means that all the compounds are initialized, even those which were not experimentally detected (see text for details). "Init CO" is like "No init" but with CO initialized. "Init PPN" is like "No init" but with PPN initialized . "Init PPN+DCB" is like "No init" but with PPN, DCB1, DCB2 and DCB3 initialized. "Init selection" is like "No init" but with PPN, DCB1, DCB2, DCB3, MGLY and PAN initialized. The curves corresponding to "Full init" and "Init selection" are close to be superimposed.
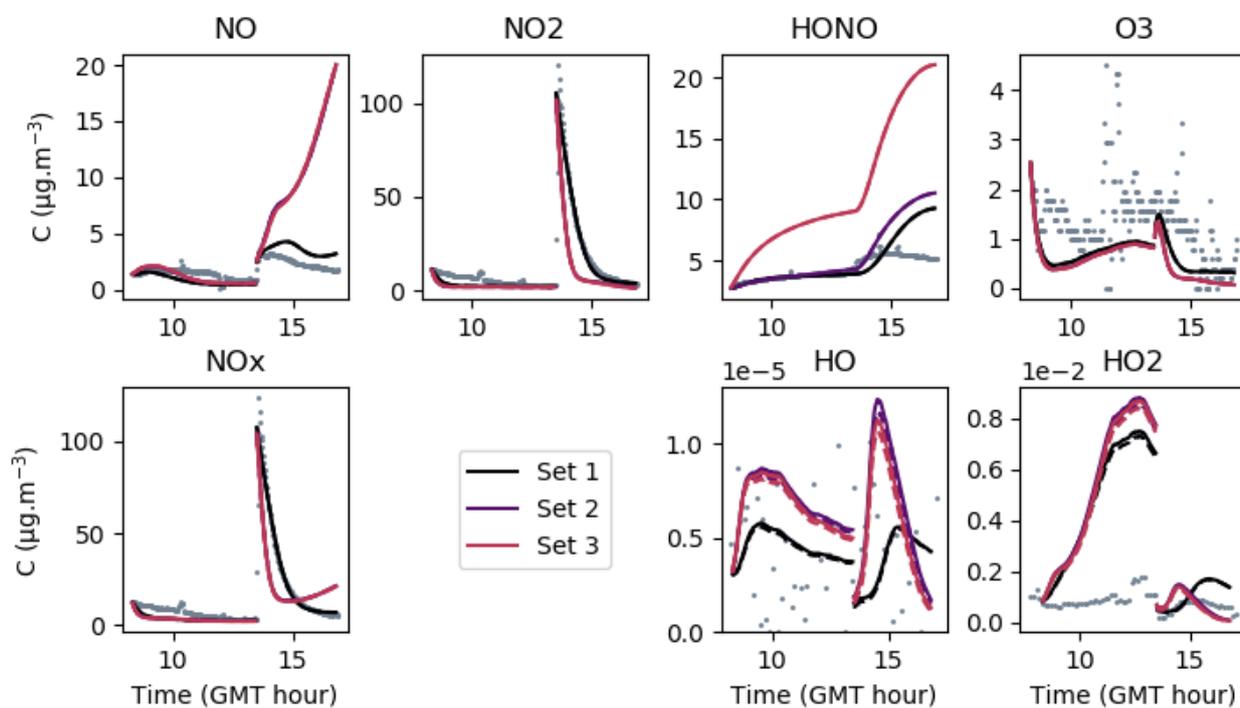
Figure 6. Simulation of Experiment 1 for the three sets of parameters. The dots denote the experimental records, the solid lines denote the concentrations simulated in the sunlit box, the dashed lines denote the concentrations in the shaded box.
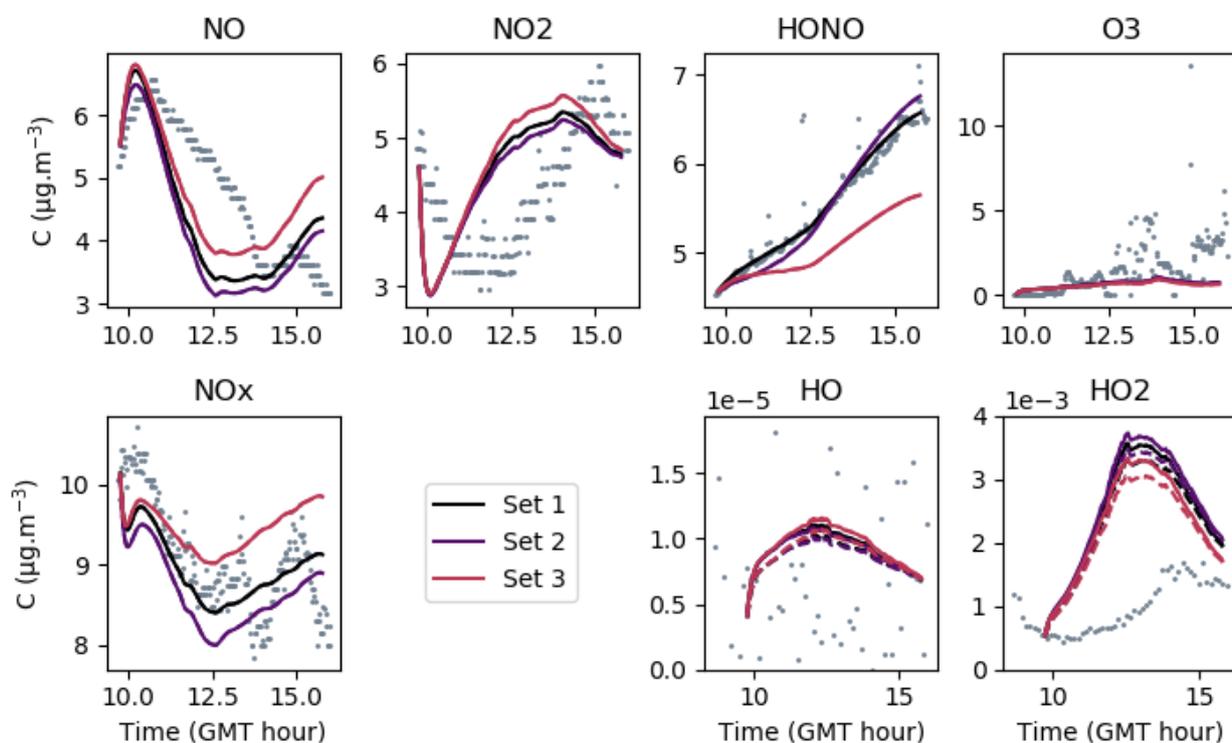
Figure 7. Simulation of Experiment 2 for the three sets of parameters. The dots denote the experimental records, the solid lines denote the concentrations simulated in the sunlit box, the dashed lines denote the concentrations in the shaded box.
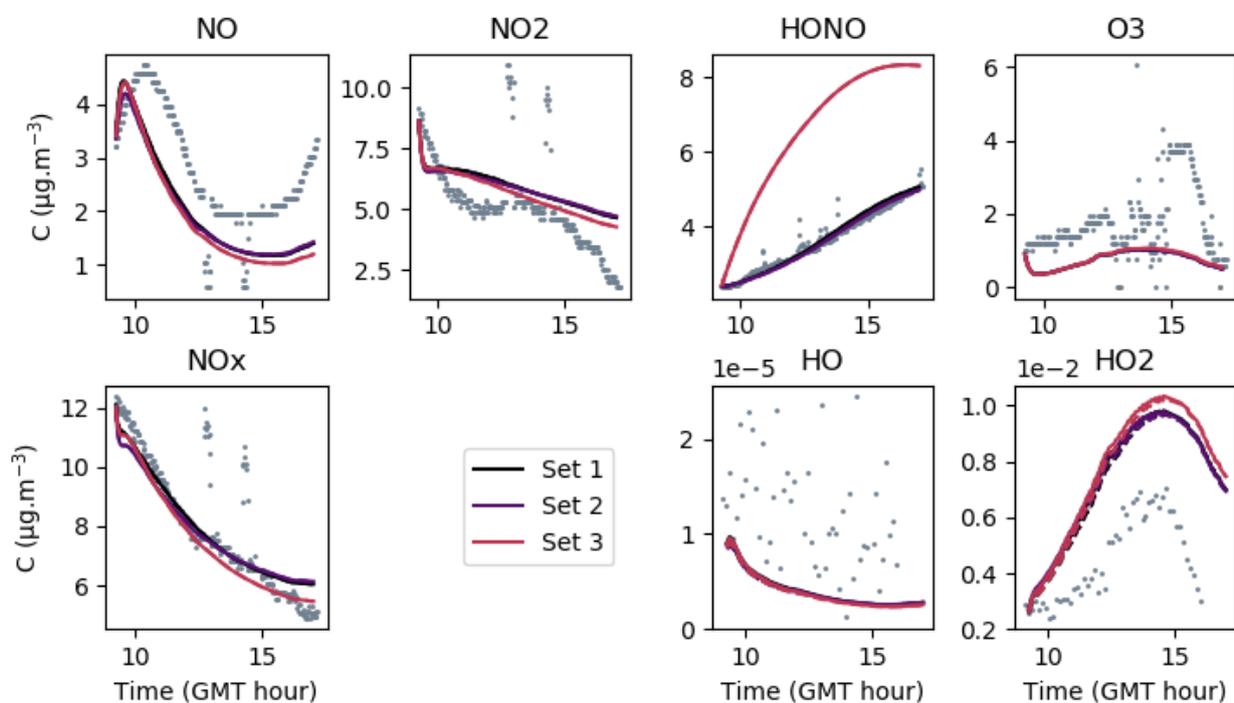
Figure 8. Simulation of Experiment 3 for the three sets of parameters. The dots denote the experimental records, the solid lines denote the concentrations simulated in the sunlit box, the dashed lines denote the concentrations in the shaded box.
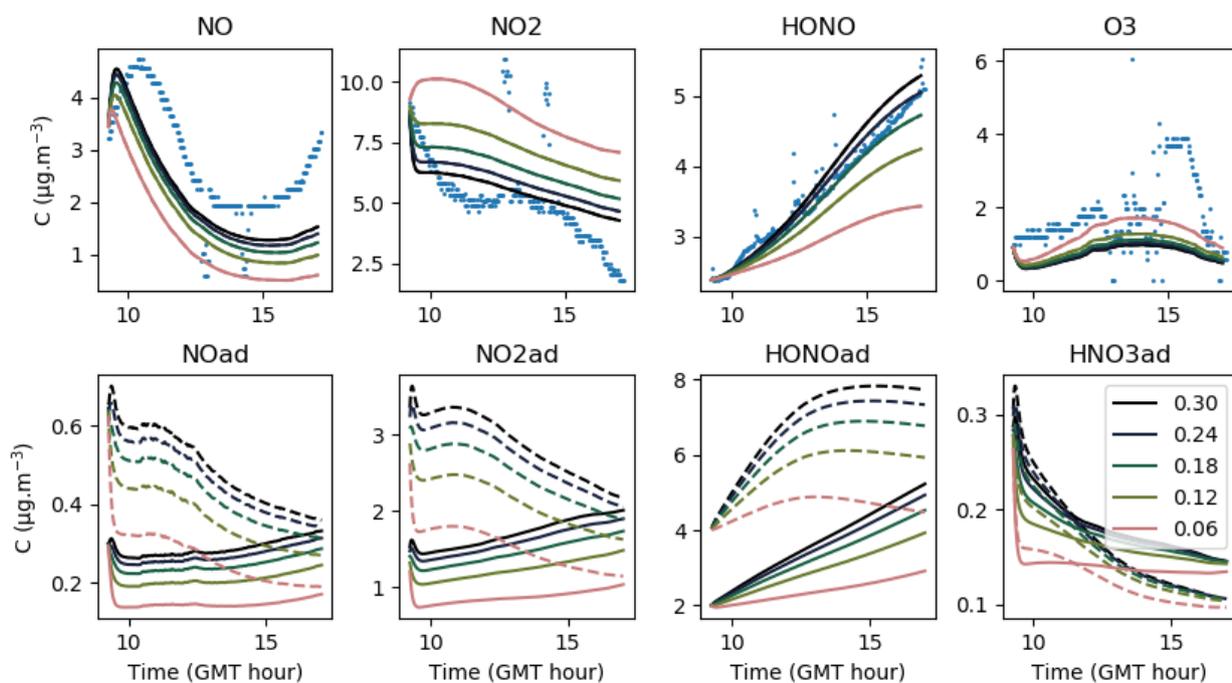
Figure 9. Gas-phase and adsorbed inorganic compounds simulated with different u_{inf}. The blue dots denote the experimental measurements (Experiment 3). The solid lines represent the concentrations in the sunlit box, the dashed lines the concentrations in the shaded box.
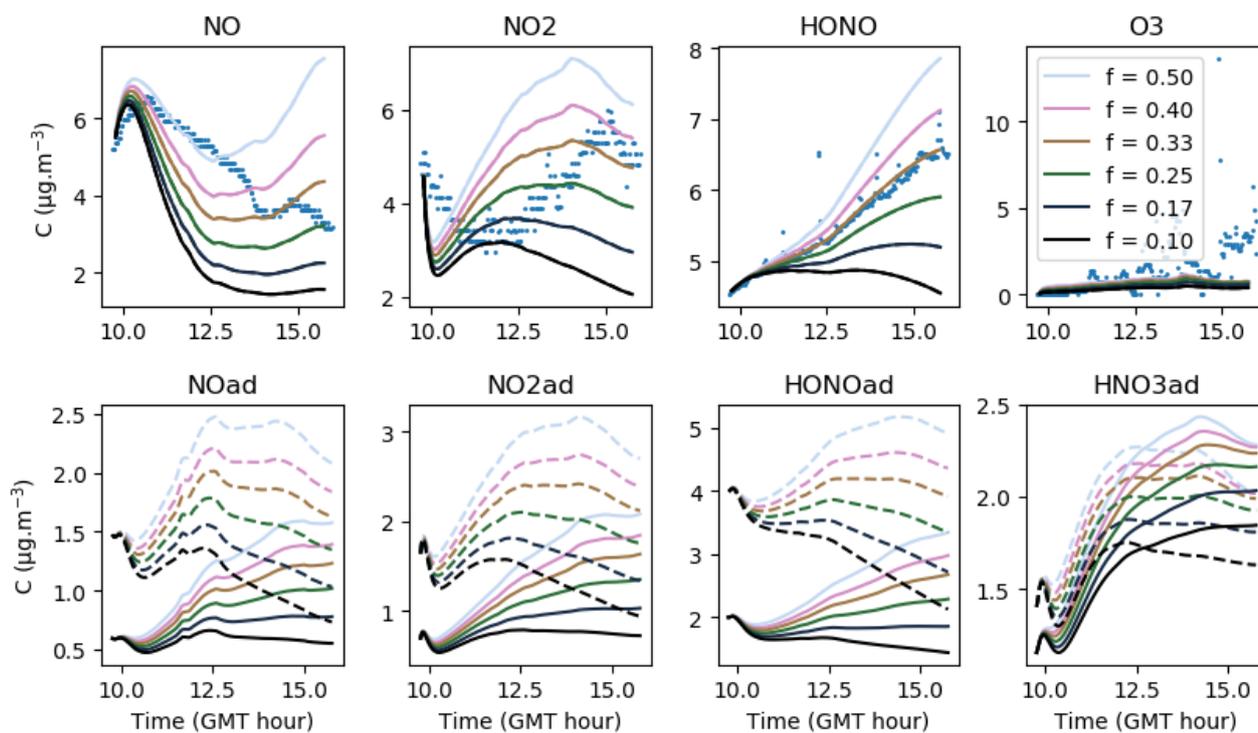
Figure 10. Gas-phase and adsorbed inorganic compounds simulated with different f. The blue dots denote the experimental measurements (Experiment 2). The solid lines represent the concentrations in the sunlit box, the dashed lines the concentrations in the shaded box.
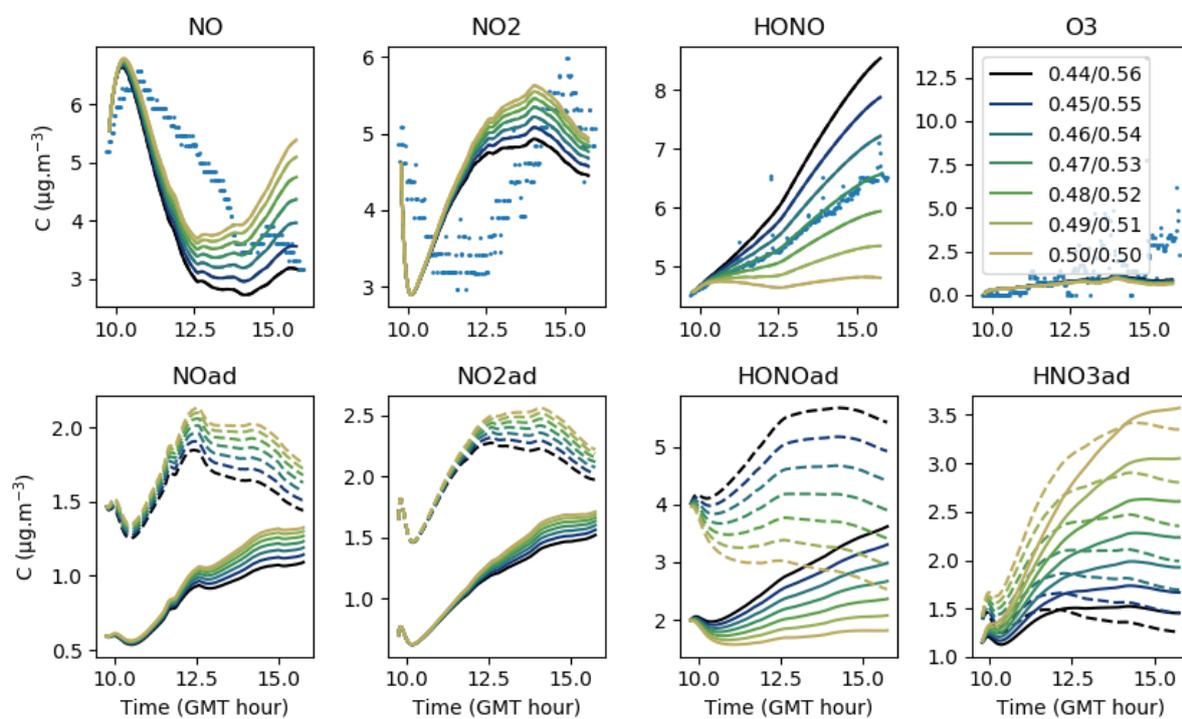
Figure 11. Gas-phase and adsorbed inorganic compounds simulated for different $\beta_{HNO_3}/\beta_{HONO}$, with $\beta_{HNO_3}/\beta_{HONO} < 1$. The blue dots denote the experimental measurements (Experiment 2). The solid lines represent the concentrations in the sunlit box, the dashed lines the concentrations in the shaded box.
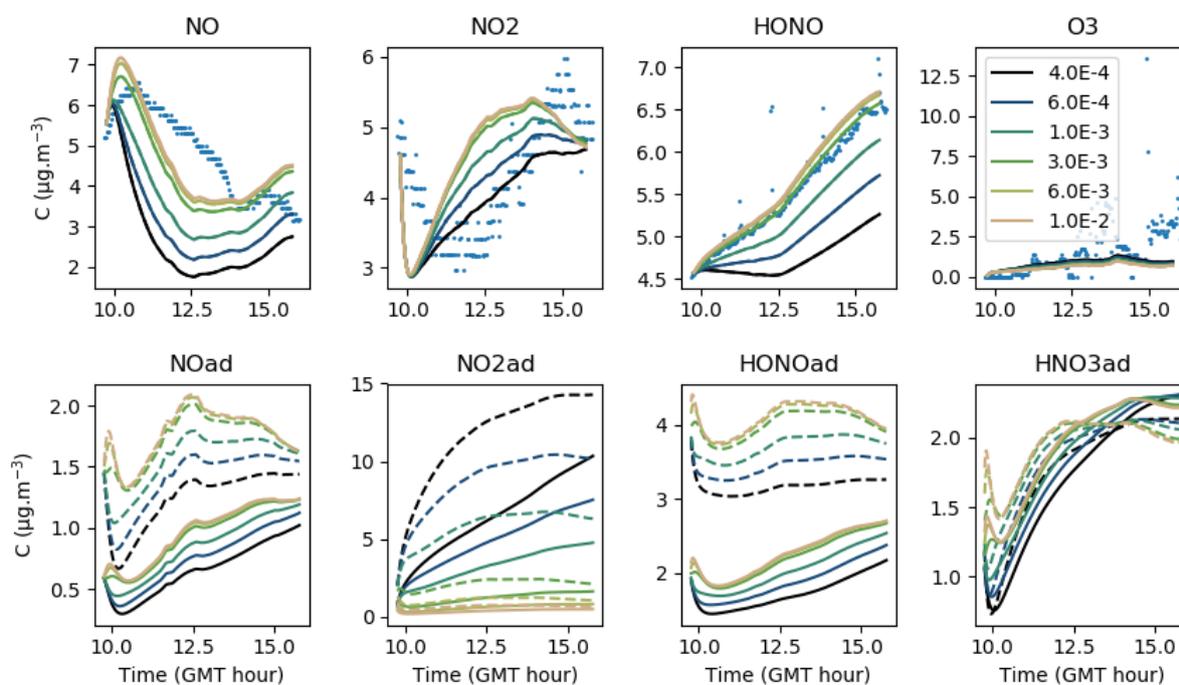
Figure 12. Gas-phase and adsorbed inorganic compounds simulated for different k_{S1}. The blue dots denote the experimental measurements (Experiment 2). The solid lines represent the concentrations in the sunlit box, the dashed lines the concentrations in the shaded box.
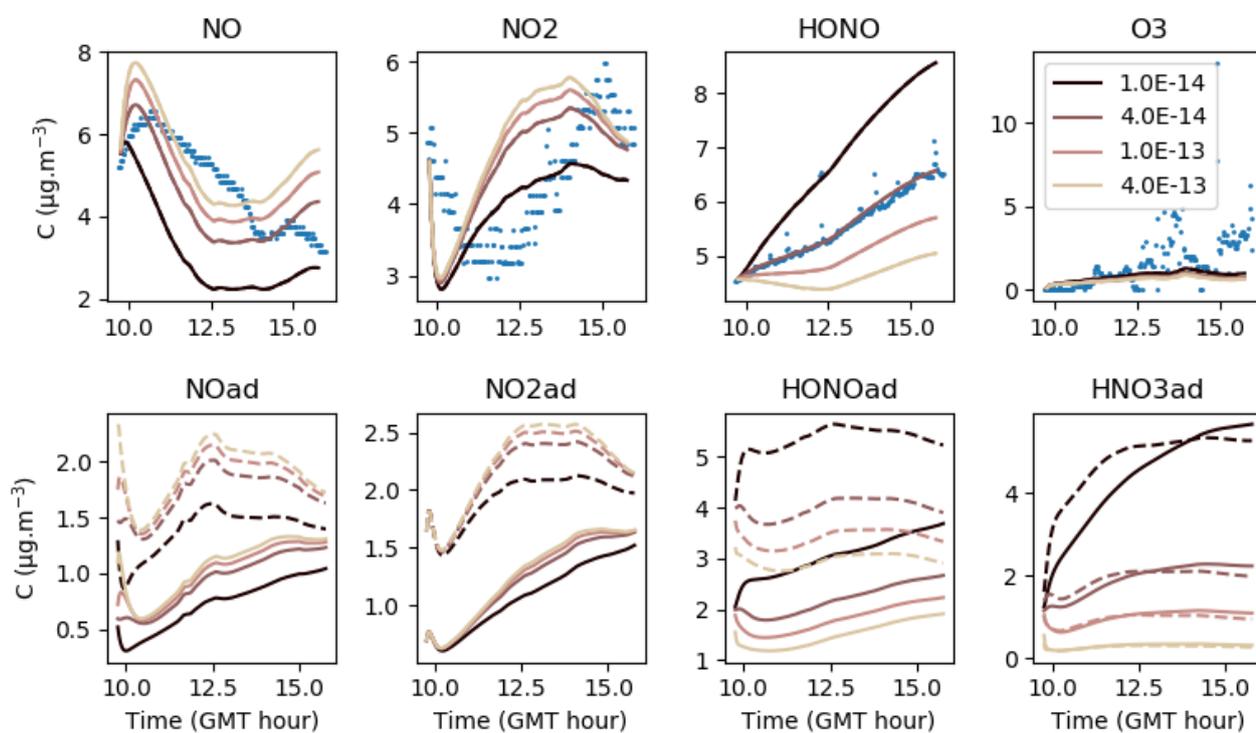
Figure 13. Gas-phase and adsorbed inorganic compounds simulated for different k_{S2}. The blue dots denote the experimental measurements (Experiment 2). The solid lines represent the concentrations in the sunlit box, the dashed lines the concentrations in the shaded box.
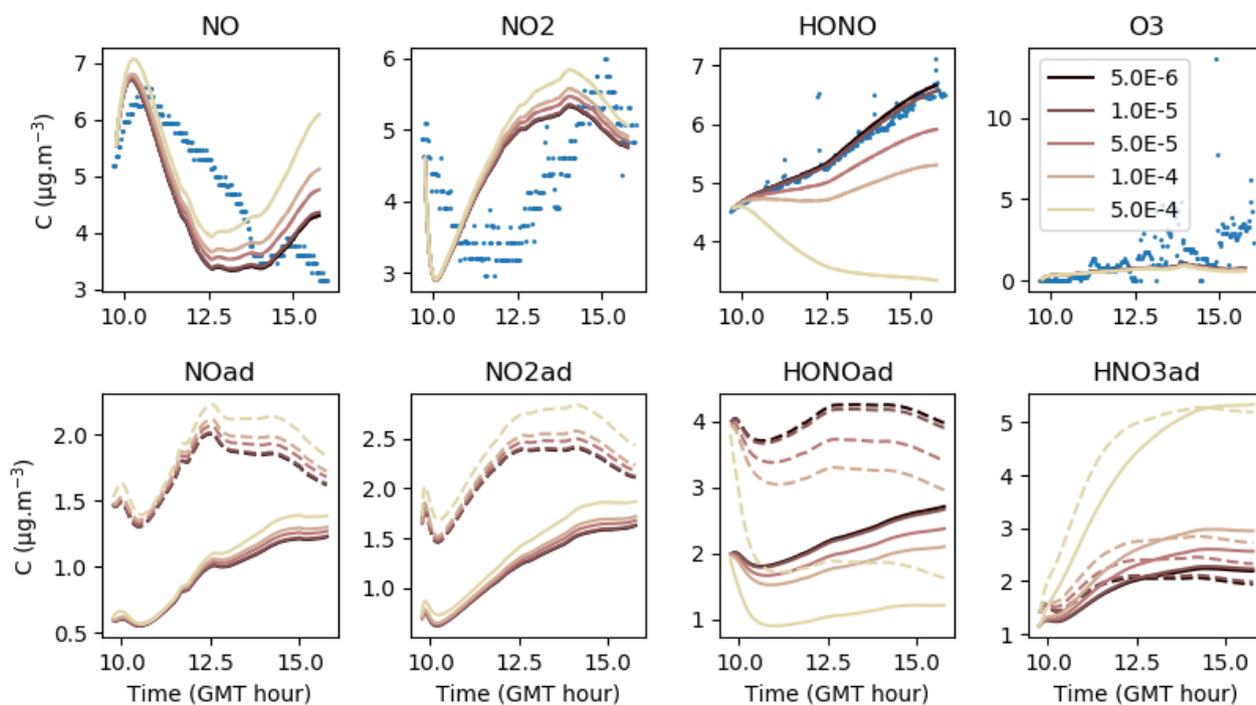
Figure 14. Gas-phase and adsorbed inorganic compounds simulated for different k_{S3}. The blue dots denote the experimental measurements (Experiment 2). The solid lines represent the concentrations in the sunlit box, the dashed lines the concentrations in the shaded box.
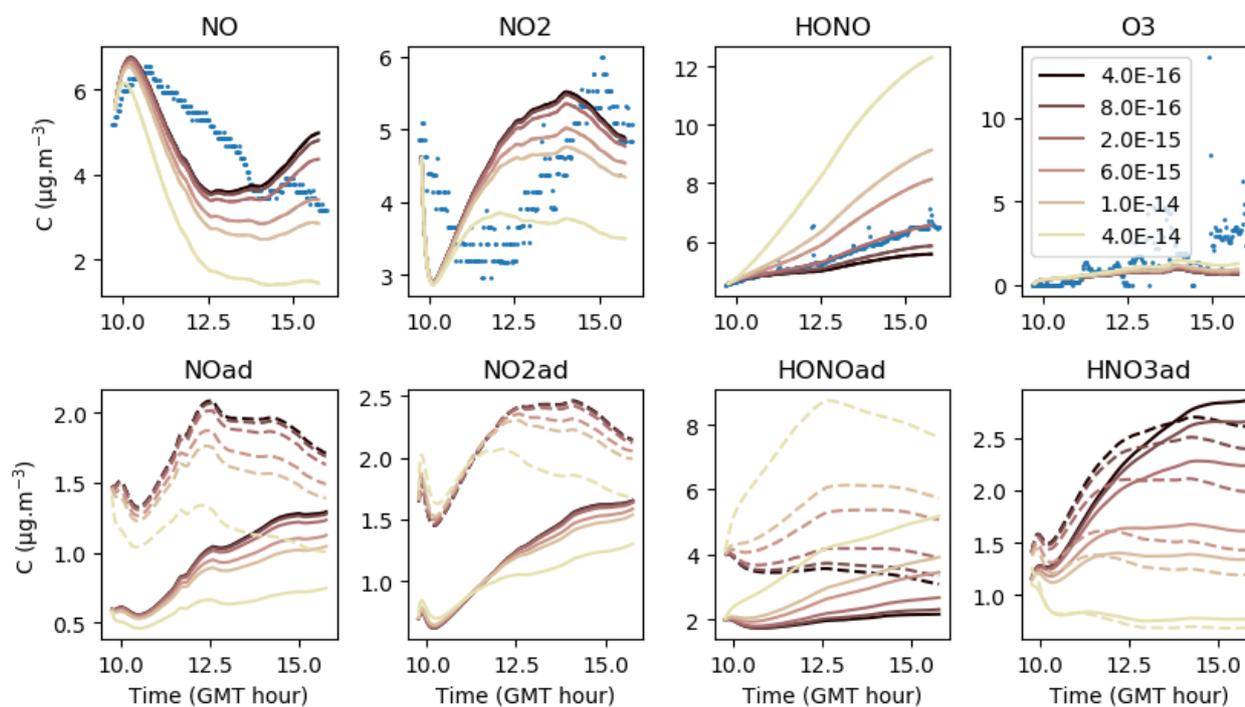
Figure 15. Gas-phase and adsorbed inorganic compounds simulated for different k_{S4}. The blue dots denote the experimental measurements (Experiment 2). The solid lines represent the concentrations in the sunlit box, the dashed lines the concentrations in the shaded box.
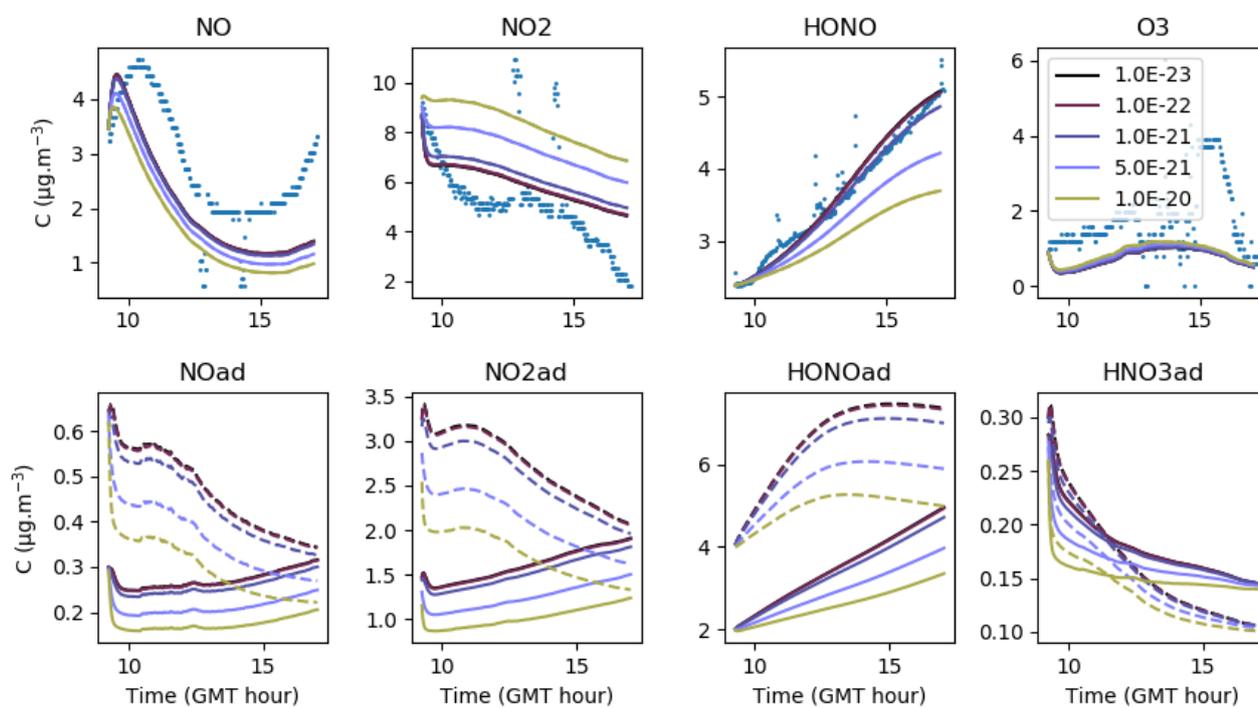
Figure 16. Gas-phase and adsorbed inorganic compounds simulated for different $k'_{NO_2\,(ad)}$. The blue dots denote the experimental measurements (Experiment 3). The solid lines represent the concentrations in the sunlit box, the dashed lines the concentrations in the shaded box.
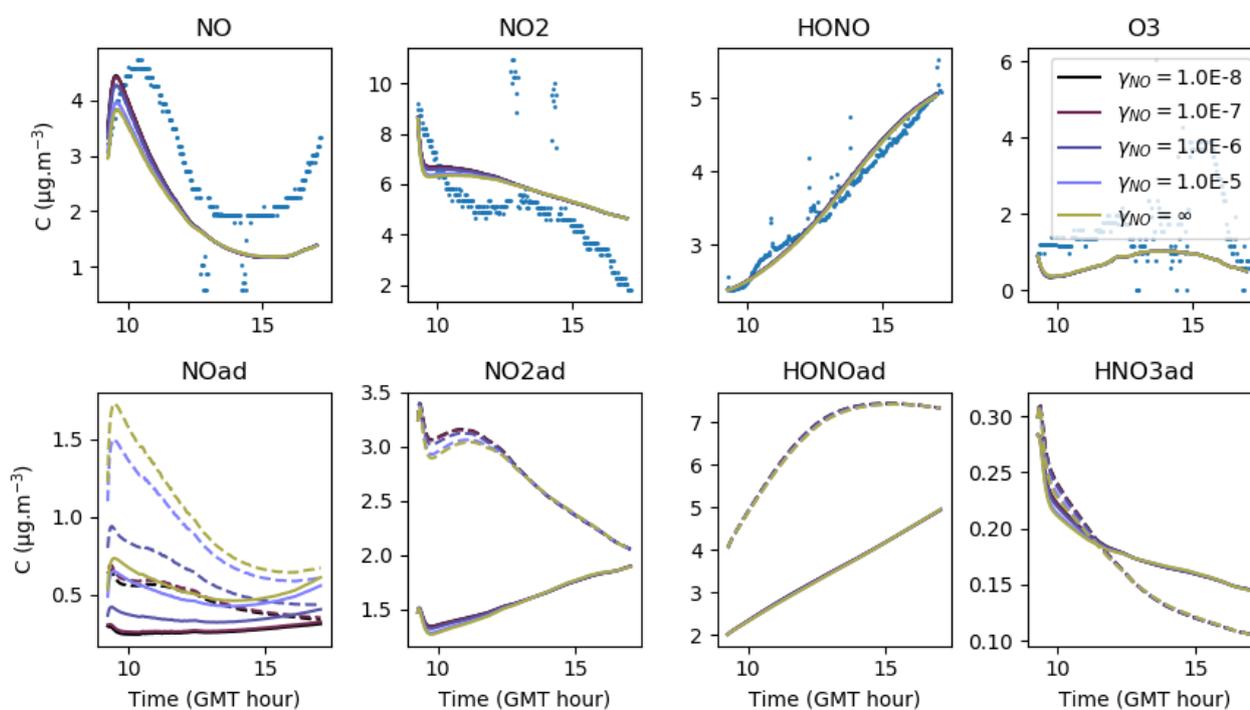
Figure 17. Gas-phase and adsorbed inorganic compounds simulated for different γ_{NO}. The blue dots denote the experimental measurements (Experiment 3). The solid lines represent the concentrations in the sunlit box, the dashed lines the concentrations in the shaded box.
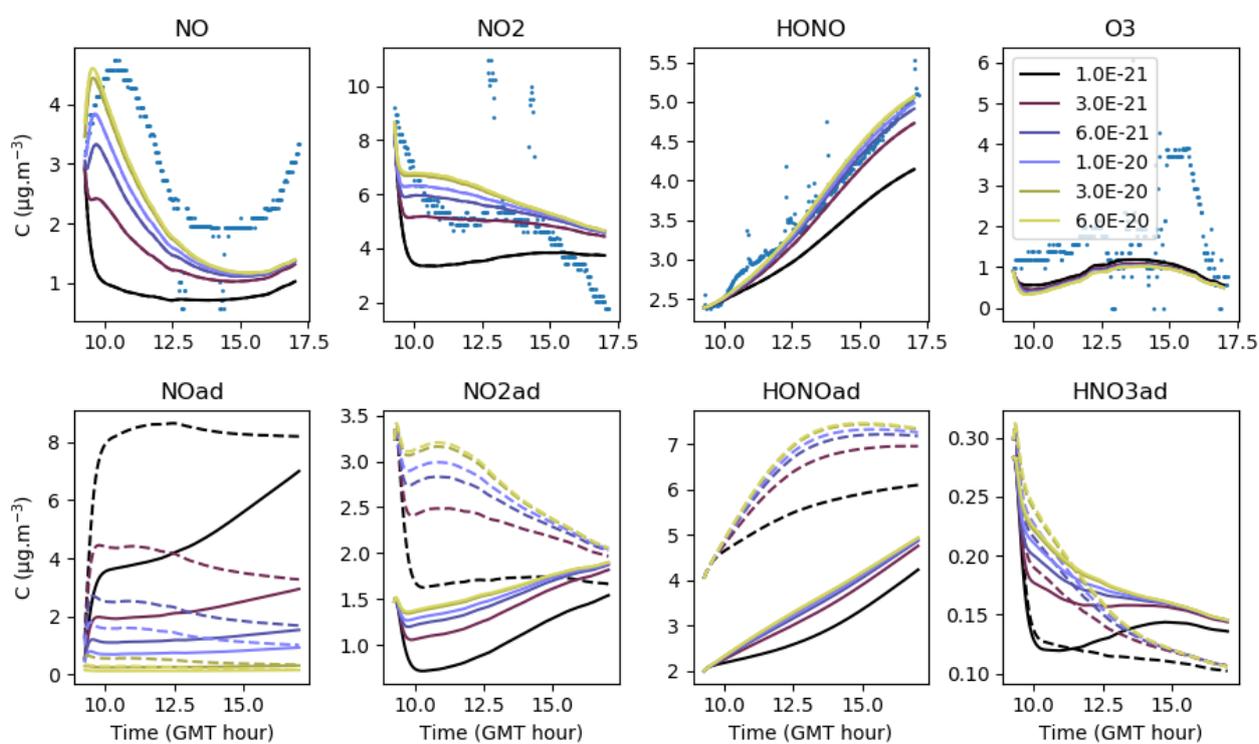
Figure 18. Gas-phase and adsorbed inorganic compounds simulated for different $k'_{NO\,(ad)}$. The blue dots denote the experimental measurements (Experiment 3). The solid lines represent the concentrations in the sunlit box, the dashed lines the concentrations in the shaded box.
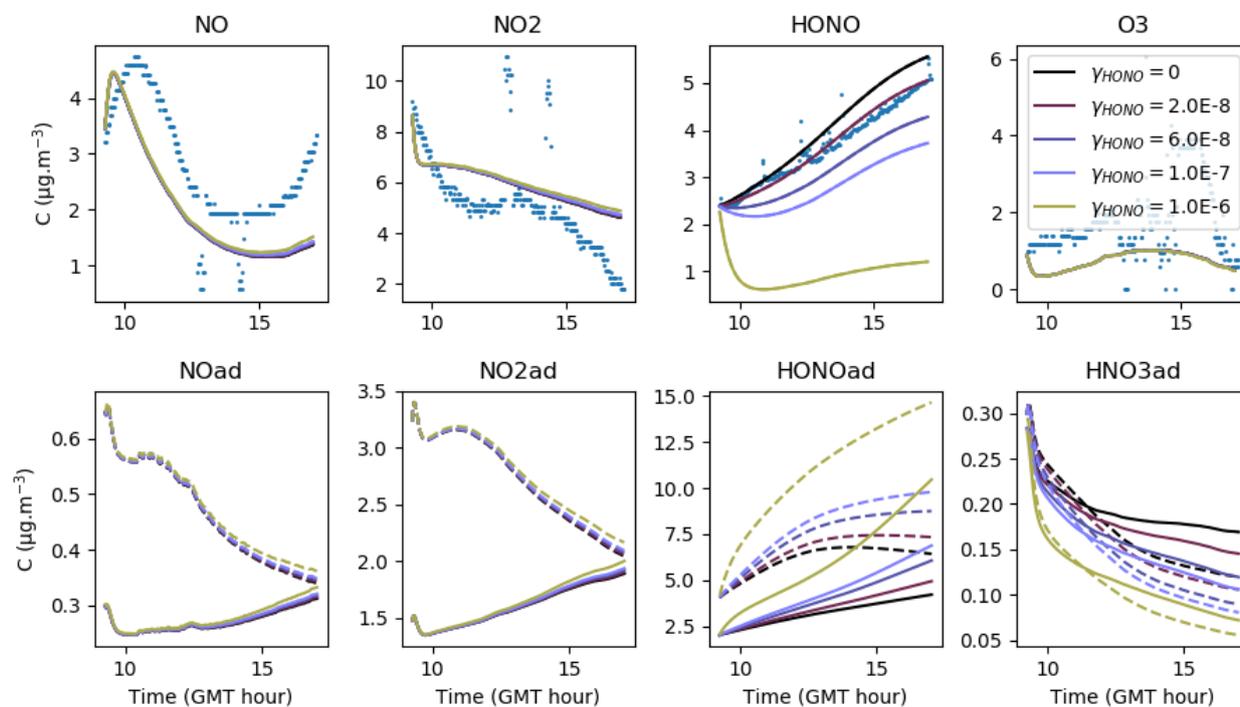
Figure 19. Gas-phase and adsorbed inorganic compounds simulated for different γ_{HONO}. The blue dots denote the experimental measurements (Experiment 3). The solid lines represent the concentrations in the sunlit box, the dashed lines the concentrations in the shaded box.
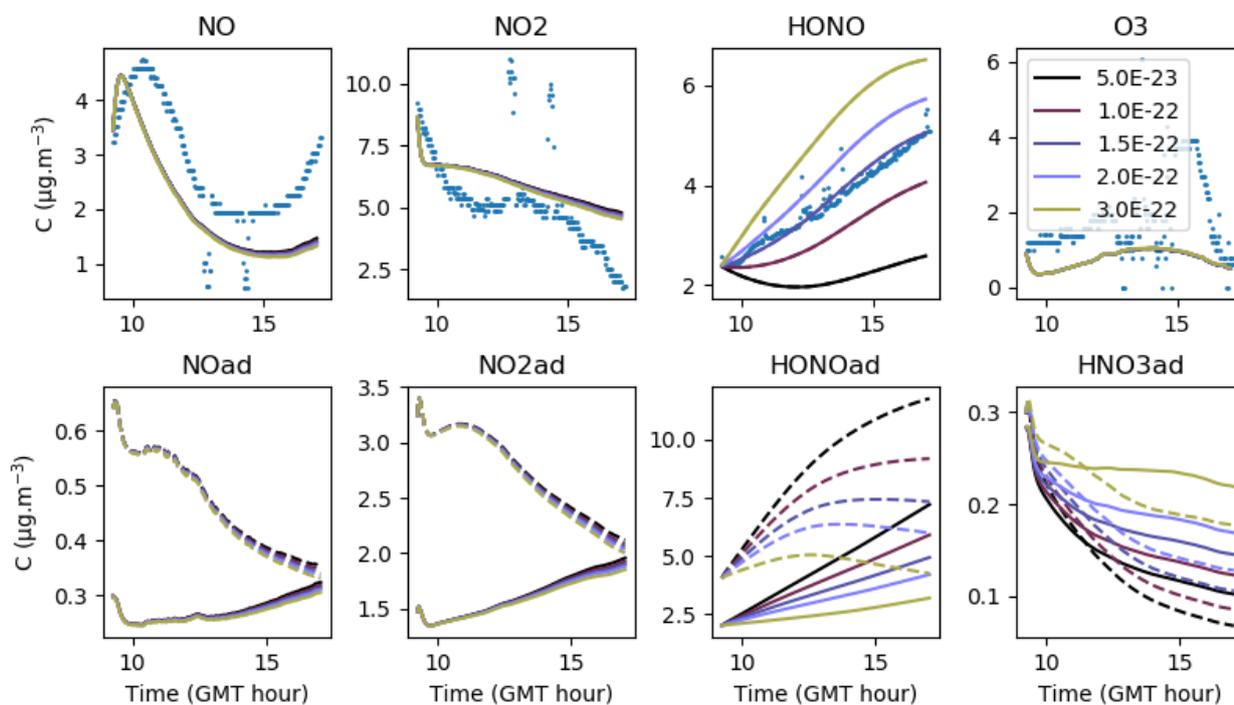
Figure 20. Gas-phase and adsorbed inorganic compounds simulated for different $k'_{HONO\,(ad)}$. The blue dots denote the experimental measurements (Experiment 3). The solid lines represent the concentrations in the sunlit box, the dashed lines the concentrations in the shaded box.
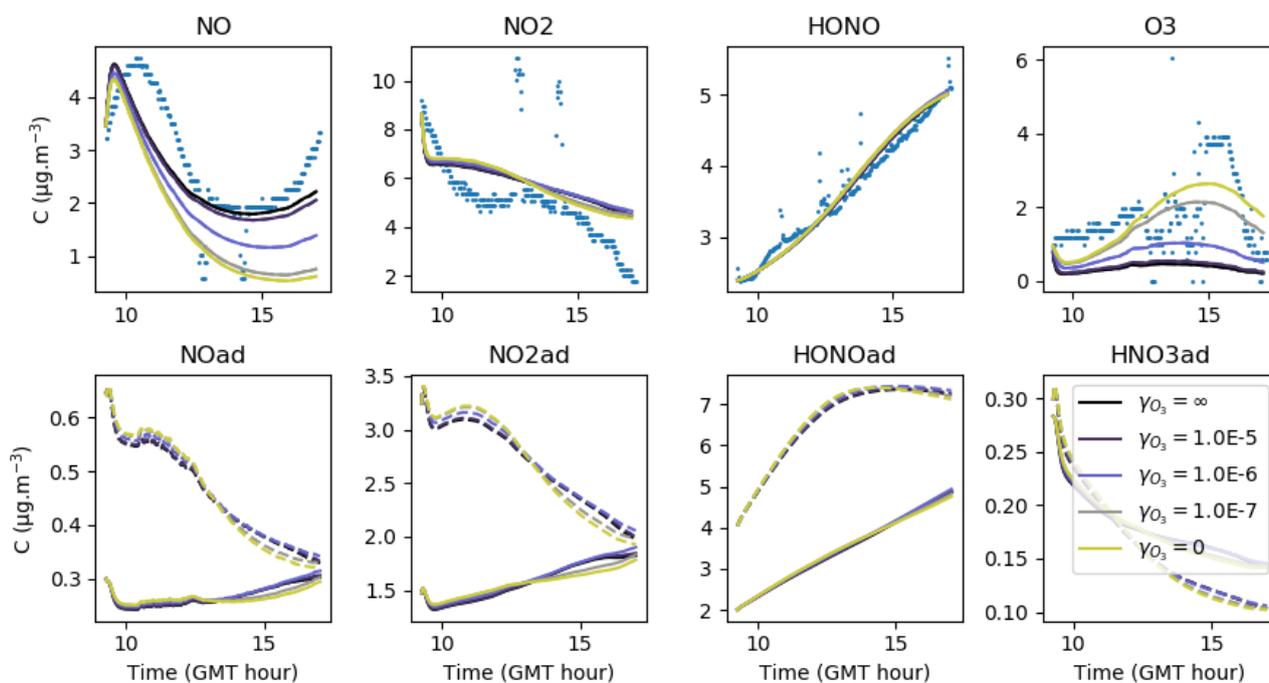
Figure 21. Gas-phase and adsorbed inorganic compounds simulated for different γ_{O_3}. The blue dots denote the experimental measurements (Experiment 3). The solid lines represent the concentrations in the sunlit box, the dashed lines the concentrations in the shaded box.
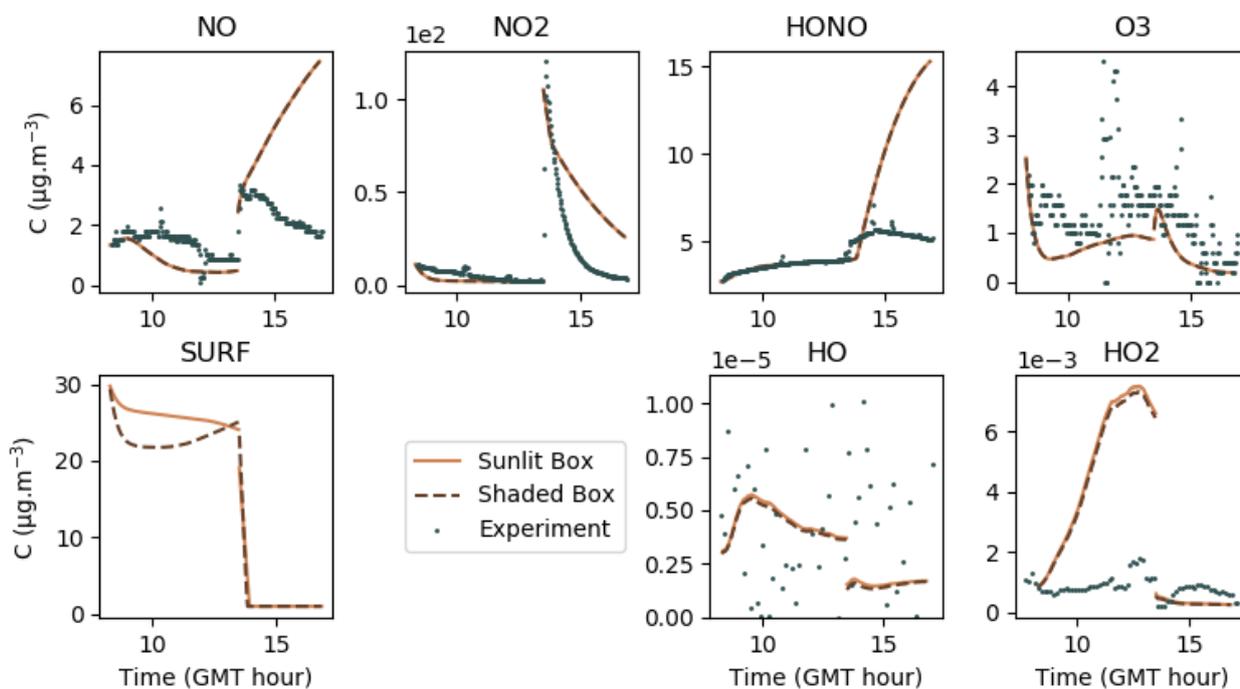
Figure 22. Implementation of a surface saturation effect using the compound SURF. The dots denote the experimental records, the solid lines denote the concentrations simulated in the sunlit box, the dashed lines denote the concentrations in the shaded box.

Appendix A: HO and HO$_2$ concentration profiles
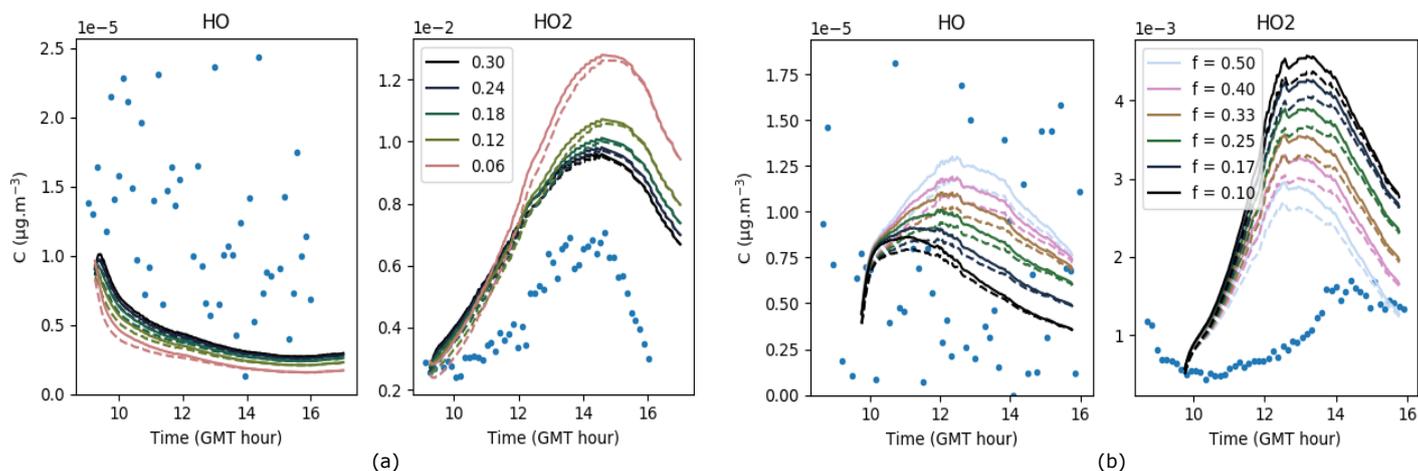
Figure A1. HO and HO$_2$ concentration profiles of the simulations presented in section 5. Variations (a) with u_{inf} (Fig. 9); (b) with f (Fig. 10). The dots denote the experimental records, the solid lines denote the concentrations simulated in the shaded box, the dashed lines denote the concentrations in the sunlit box.
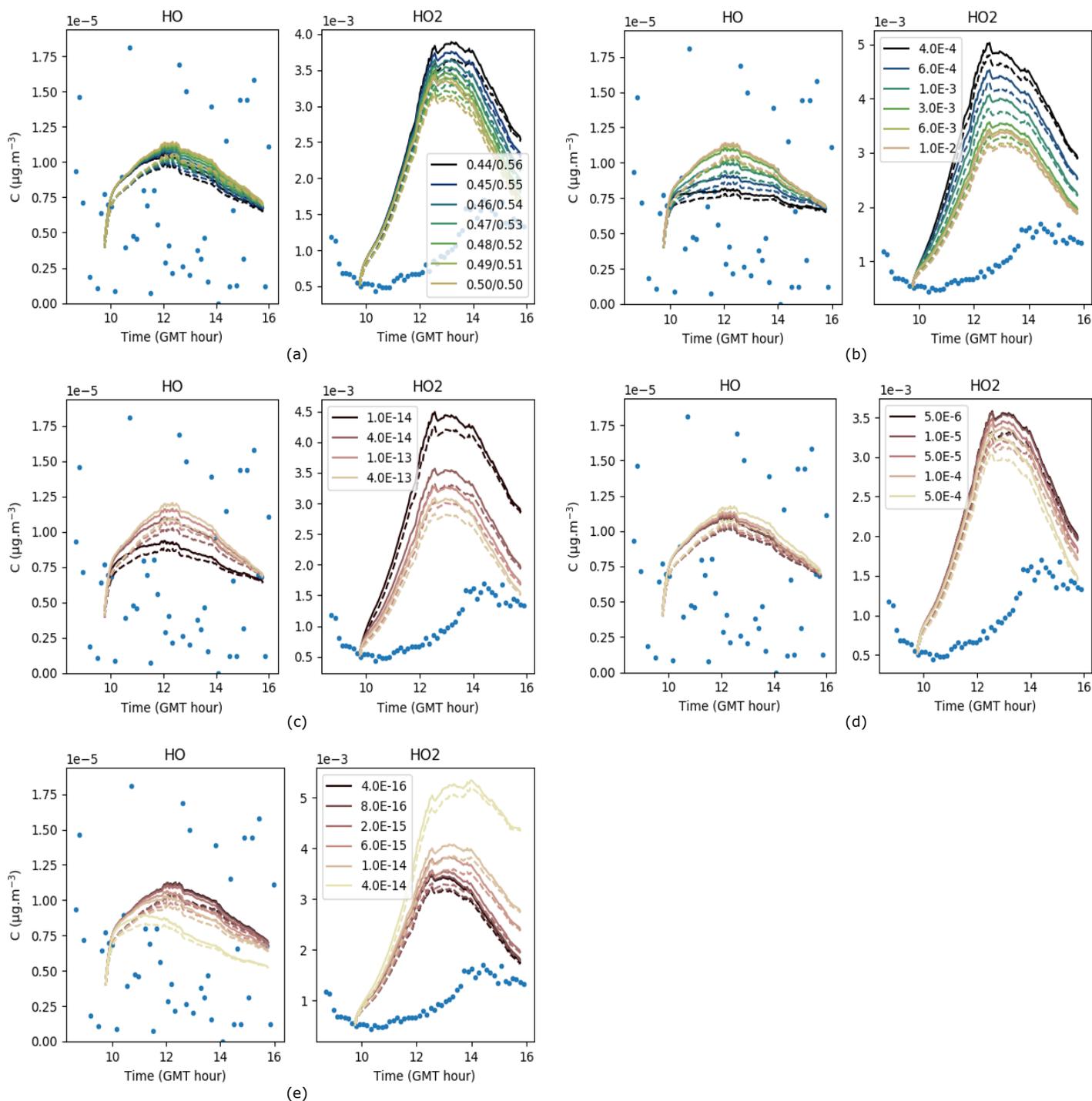
Figure A2. HO and HO$_2$ concentration profiles of the simulations presented in section 5. Variations (a) with $\beta_{\text{HNO}_3}/\beta_{\text{HONO}}$ (Fig. 11); (b) with k_{S1} (Fig. 12); (c) with k_{S2} (Fig. 13); (d) with k_{S3} (Fig. 14); (e) with k_{S4} (Fig. 15). The dots denote the experimental records, the solid lines denote the concentrations simulated in the shaded box, the dashed lines denote the concentrations in the sunlit box.
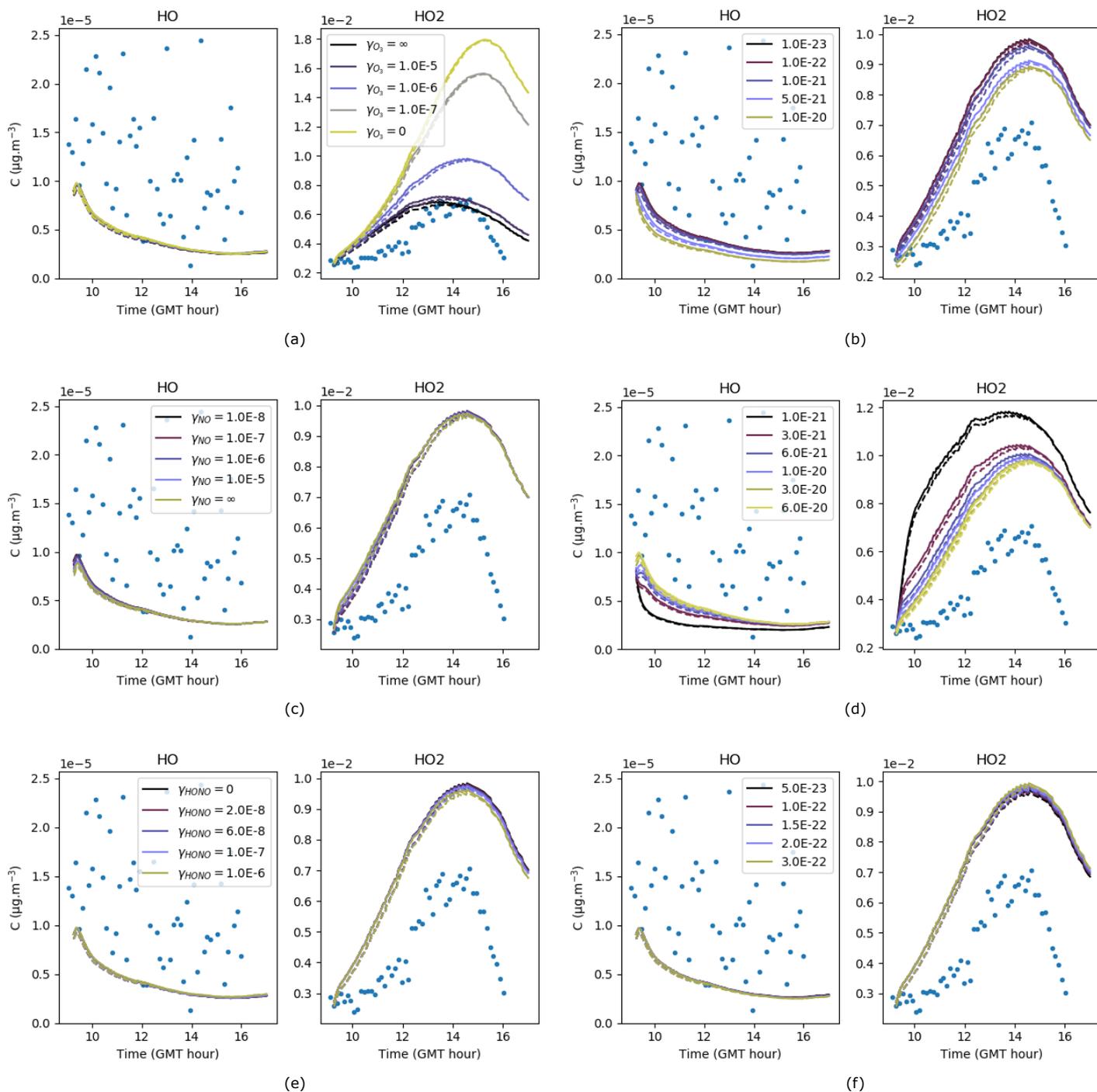
Figure A3. HO and HO$_2$ concentration profiles of the simulations presented in section 5. Variations (a) with γ_{O_3} (Fig. 21); (b) with $k'_{NO_2\,(ad)}$ (Fig. 16); (c) with γ_{NO} (Fig. 17); (d) with $k'_{NO\,(ad)}$ (Fig. 18); (e) with γ_{HONO} (Fig. 19); (f) with $k'_{HONO\,(ad)}$ (Fig. 20). The dots denote the experimental records, the solid lines denote the concentrations simulated in the shaded box, the dashed lines denote the concentrations in the sunlit box.